# Potential of mm-Wave Doppler-Polarimetric Profiler Observations for Quality Assessment of Hydrometeor Classification Schemes

Bogerd, L.; Leijnse, H.; Overeem, A.; Unal, C. M.H.; Uijlenhoet, R.; van der Veen, S.

**DOI**
10.1029/2024JD042398

**Publication date**
2025

**Document Version**
Final published version

**Published in**
Journal of Geophysical Research: Atmospheres

AGU ADVANCING EARTH AND SPACE SCIENCES

JGR Atmospheres

RESEARCH ARTICLE
10.1029/2024JD042398

# Potential of mm-Wave Doppler-Polarimetric Profiler Observations for Quality Assessment of Hydrometeor Classification Schemes

L. Bogerd[1,2], H. Leijnse[2], A. Overeem[2,3], C. M. H. Unal[4], R. Uijlenhoet[3], and S. van der Veen[5]

[1]Hydrology and Environmental Hydraulics Group, Wageningen University and Research, Wageningen, The Netherlands, [2]R&D Observations and Data Technology, Royal Netherlands Meteorological Institute (KNMI), De Bilt, The Netherlands, [3]Department of Water Management, Faculty of Civil Engineering & Geosciences, Delft University of Technology, Delft, The Netherlands, [4]Department of Geoscience and Remote Sensing, Faculty of Civil Engineering & Geosciences, Delft University of Technology, Delft, The Netherlands, [5]R&D Weather and Climate Modelling, Royal Netherlands Meteorological Institute (KNMI), De Bilt, The Netherlands

**Key Points:**

- Combining spectral polarimetric observations and radar-based hydrometeor classification to gain insights into hydrometeor properties
- Comprehensive analysis of Doppler spectra over a midlatitude region for six cases
- Dual wavelength ratio can be used to identify radial wind component and extract terminal fall velocities during stratiform events

**Correspondence to:**
L. Bogerd,
linda.bogerd@wur.nl

**Citation:**
Bogerd, L., Leijnse, H., Overeem, A., Unal, C. M. H., Uijlenhoet, R., & van der Veen, S. (2025). Potential of mm-wave Doppler-polarimetric profiler observations for quality assessment of hydrometeor classification schemes. *Journal of Geophysical Research: Atmospheres*, *130*, e2024JD042398. https://doi.org/10.1029/2024JD042398

Received 4 SEP 2024
Accepted 14 MAY 2025

## Abstract

Dual-polarization weather radars have improved the accuracy of precipitation estimates. However, challenges persist in evaluating hydrometeor classification (HMC) algorithms, thereby impacting the accuracy of precipitation estimates. This study proposes to use full Doppler spectra in both polarizations from a Ka- and W-band Doppler-polarimetric profiler with a 45° elevation angle to provide insights into hydrometeor characteristics. A novel methodology was developed to link the observed spectra with the output of an HMC scheme. We applied the wradlib HMC scheme using C-band weather radar data from the Netherlands for six cases (2021–2022). The HMC scheme output is used to calculate mixing ratios that are combined with the corresponding scattering properties using the Atmospheric Radiative Transfer Simulator microwave single scattering properties database (frozen hydrometeors) and T-matrix calculations (liquid hydrometeors) to simulate Doppler spectra of polarimetric variables that would be measured by the profiler. Comparing these simulations with actual profiler measurements enables a quality assessment. The method works in stratiform cases, but convective cases reveal the influence of turbulence and wind variability. Uncertainty arises from the selection of specific parameterizations for the particle size distribution and the relationship between hydrometeor size and terminal fall velocity as well as from the derived mixing ratios. Additionally, the 45° angle complicates separating horizontal wind from hydrometeor fall velocities, although the Mie notch in the dual-wavelength ratio can be effectively used to remove the radial wind component. Our results underline limitations that must be addressed but also show that integrating spectral and dual-frequency observations could yield valuable insights into hydrometeor characteristics.

## Plain Language Summary

The identification of precipitation type, such as snow, rain, and hail, improves the retrieval of radar-based precipitation estimates. However, correct identification of precipitation types and their characteristics with operational weather radar observations remains difficult. In this study, we investigate the potential of using profiling radar observations to uncover hydrometeor characteristics. In particular, we explore the possibility of integrating these observations with a hydrometeor classification scheme derived from operational weather radars in the Netherlands aiming to assess the performance of the classification scheme. The profiler Doppler spectra provide a comprehensive view of the full range of fall velocities observed within a single radar bin, offering detailed insights into hydrometeor characteristics and their variability within that bin. The method works well for precipitation with limited spatiotemporal variability but has a lower performance for highly variable events, such as thunderstorms. Additionally, the profiler's elevation angle complicates separating the fall velocity from wind. However, using the two frequency channels of the profiler shows promising results in correcting for the wind influence.

## 1. Introduction

The widespread use of dual-polarization (dual-pol) radars has significantly advanced weather observation especially for precipitation (Cifelli & Chandrasekar, 2010). Unlike conventional radars that transmit linearly polarized electromagnetic signals at a single (typically horizontal) polarization, dual-pol radars transmit and receive signals at both vertical and horizontal polarizations (Bringi & Chandrasekar, 2001; Ryzhkov &

Zrnic, 2019). This capability allows them to reveal information regarding the vertical and horizontal dimensions of the objects, such as hydrometeors, in the measurement volume.

Combining the backscattered signals at orthogonal observations enables the identification of hydrometeor properties, such as hydrometeor type (Al-Sakka et al., 2013). Furthermore, dual-pol observations assist in identifying and removing nonmeteorological echoes, such as birds, insects, and ground clutter (Chen et al., 2022; Fabry, 2015; Fukao et al., 2014), and estimate and correct for rain-induced attenuation along the radar beam (e.g., Overeem et al., 2021; Ryzhkov et al., 2014). These implementations enhance the accuracy of quantitative precipitation estimates and forecasts (QPE and QPF, respectively) resulting in better warnings. Hence, in addition to horizontal reflectivity ($Z_H$), many precipitation retrieval and classification algorithms employ dual-pol variables, in particular differential reflectivity ($Z_{DR}$), representing the ratio of horizontal to vertical reflectivity, co-polar correlation coefficient $(\rho_{HV})$, indicating the similarity of the horizontally and vertically polarized returned signals; and specific differential phase $(K_{DP})$ estimated from the phase shift difference between horizontally and vertically polarized signals (Fabry, 2015; Kumjian, 2018; Rauber & Nesbitt, 2018).

In this study, we explore the information contained in profiler observations and assess their potential for evaluating applications such as dual-polarization hydrometeor classification (HMC) schemes. Profiler observations provide continuous, high-resolution data, thereby addressing some of the limitations of conventional methods used to derive hydrometeor characteristics and evaluate HMC schemes. For example, current methods often rely on measurements from aircraft and drifting balloons (Lim et al., 2005; Liu & Chandrasekar, 2000; Schuur et al., 2003). These measurements provide only snapshots, which are challenging to match with radar observations, particularly when the radar operates in scanning mode. These discrepancies become even larger during small-scale short-lived convective events (Berne et al., 2004; Bogerd et al., 2024; Chaubey et al., 1999). Additionally, these methods disturb the observation field. Studies using radar observations employed data from radars operating at the same frequency as input (Falconi et al., 2015; Schmidt et al., 2018) not yielding an independent evaluation as those observations are confronted with the same challenges as those that are evaluated. Evaluation has also been performed using 2D video disdrometers (Besic et al., 2016; Grazioli et al., 2015), but these only offer point measurements at ground-level, resulting in limited spatial representativeness.

Profiler observations address these challenges. Hence, we identify the information content in profiler Doppler spectra and spectral polarimetry and explore their utility in assessing HMC schemes. Specifically, we compare Doppler spectra of polarimetric observables from a profiler on a slanted path to spectra simulated based on the HMC output. In principle, dual-pol measurements offer the most information when the radar is oriented horizontally, whereas vertically pointing radars are more effective for Doppler measurements (Bringi & Chandrasekar, 2001; Fabry, 2015). As a trade-off, the profiler was operated at a 45° elevation angle (Unal & Brule, 2024). To the authors' knowledge, this method has not been used previously to evaluate the performance of HMC algorithms. The technique is demonstrated using the open-source wradlib HMC scheme applied to a C-band weather radar for several case studies in the Netherlands.

To enable comparison between the HMC output and the profiler observations, several processing steps are required. First, based on the HMC output, we selected the hydrometeor type and gained the corresponding scattering properties from the open-source scattering database Atmospheric Radiative Transfer Simulator (ARTS) (Section 2.2.2). Second, mixing ratios are calculated by combining C-band reflectivity measurements with the HMC scheme output (Section 2.4). Combining the mixing ratios with scattering properties enables the construction of spectra that can be compared to the Doppler spectra from the profiler (Section 3). The discussion (Section 4) elaborates on the information content of the polarimetric profiler spectra as well as the potential of these observations to validate HMC schemes. Finally, conclusions are presented in Section 5.

## 2. Measurement and Methods

### 2.1. Research Area and Period

The Netherlands (50.78°–53.68°N, 3.38°–7.38°E; land surface area approximately 35,000 km$^2$; yearly rainfall about 900 mm) receives similar amounts of precipitation throughout its four seasons. Precipitation characteristics such as intensity, duration, and type, however, do vary with season. Summer typically experiences heavier precipitation in shorter time intervals, whereas winter precipitation tends to be more persistent but lighter in intensity. Snow occasionally reaches the ground in winter and early spring, hail is more common during summer

10.1029/2024JD042398

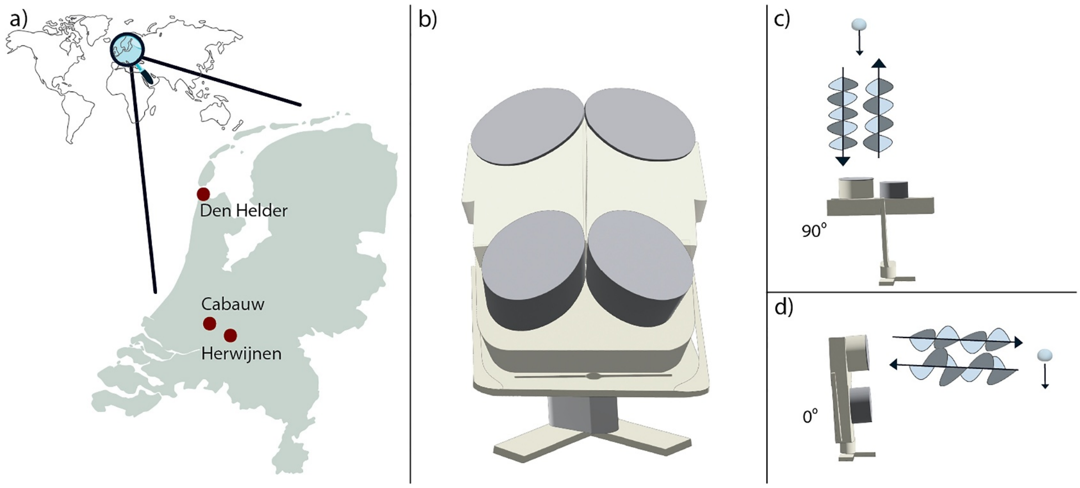


**Figure 1.** (a) Locations of the three radars: the C-band radars at Den Helder and Herwijnen, and the profiler at the Ruisdael observatory near Cabauw. (b) Illustration of the employed profiler. The lower antennas operate at 94 GHz, and the upper ones at 35 GHz. (c) A scan elevation of 90° is optimal for Doppler measurements of fall velocities. (d) A scan elevation of 0° is optimal for dual-pol measurements: the large, oblate raindrop results in a larger amplitude and phase shift in the horizontal direction (gray) compared to the vertical direction (light blue) in the returned signal.

convective events, whereas rain occurs throughout the year. More detailed descriptions of the Dutch precipitation characteristics are available in studies by Overeem et al. (2009) and Bogerd et al. (2021). Case studies from different seasons in 2021 and 2022 were selected to ensure an accurate representation of the Dutch climate.

### 2.2. Data

#### 2.2.1. Weather Radars and Profiler

*Dual-pol C-band weather radars.* The Royal Netherlands Meteorological Institute (KNMI) has two operational dual-pol C-band (wavelength 5.3 cm, frequency 5.6 GHz) weather radars: one in Herwijnen and one in Den Helder (Figure 1). Both radars scan at 15 elevation angles ranging from 0.3° to 25.0° every 5 min. The sixteenth elevation angle, 90° ("birdbath scan"), was not used in this study. More technical details regarding these radars are given by Beekhuis and Mathijssen (2018). In this study, only the radar located in Herwijnen was used due to its proximity to the Doppler-polarimetric profiler and is referred to as "C-band radar" in the remainder of this paper. The dual-pol bulk radar variables (reflectivity, mean Doppler velocity, differential reflectivity, differential phase, and copolar correlation coefficient) are available on a polar grid. The grid has an azimuth resolution of 1° while the range resolution varies with elevation (between 90 m for higher scans and 225–400 m for the lowest scans).

*Ka- and W-band Doppler-polarimetric profiler.* The dual-frequency, Doppler-polarimetric profiler (from now on referred to as "profiler") is installed at the Ruisdael Observatory in Cabauw, 20 km from the C-band radar in Herwijnen. Observations are available every 3–4 s. Although the profiler can sweep in all directions, we only used observations at a fixed elevation angle of 45°. At this angle, a component of the hydrometeor fall velocities is captured in the Doppler information while at the same time polarimetric variables can be obtained, which give meaningful information about hydrometeor shapes (Figure 1). The profiler is a frequency-modulated continuous wave (FMCW) radar operating at Ka-band (wavelength 8.6 mm, frequency 35 GHz) and W-band (wavelength 3.2 mm, frequency 94 GHz). The beamwidth is 0.84° and 0.56° for 35 and 94 GHz, respectively. The higher frequency compared to the C-band radars allows for the detection of smaller hydrometeors (Kollias et al., 2011) but also leads to more attenuation during heavier precipitation events.

The profiler's distinct advantage is that it stores full Doppler spectra for both polarizations, enabling us to obtain detailed information on hydrometeor characteristics and particle size distributions (PSDs). The FMCW profiler employs three different chirps that allow for different specifications with height. For a fixed chirp, the number of consecutive chirps and the chirp duration determine the Doppler velocity resolution and the maximum unambiguous Doppler velocity (Table 1). The latter defines the range of Doppler velocities measurable without aliasing. Additionally, for the Doppler processing, a Fast Fourier Transform windowing function is applied that

**Table 1**
*Profiler's Resolutions and Maximum Doppler Velocities are Defined for Each Chirp*

| | Chirp [-] | Velocity res. [m $s^{-1}$] | Unamb. velocity [m $s^{-1}$] | Range res. [m] |
|---|---|---|---|---|
| **2021** | | | | |
| 35 GHz | 1 | 0.15 | 19.73 | 29.81 |
| | 2 | 0.13 | 16.08 | 29.81 |
| | 3 | 0.17 | 10.66 | 55.04 |
| 94 GHz | 1 | 0.06 | 7.35 | 29.81 |
| | 2 | 0.05 | 5.99 | 29.81 |
| | 3 | 0.06 | 3.97 | 55.04 |
| **2022** | | | | |
| 35 GHz | 1 | 0.19 | 24.19 | 29.81 |
| | 2 | 0.07 | 18.36 | 29.81 |
| | 3 | 0.20 | 12.58 | 55.04 |
| 94 GHz | 1 | 0.07 | 9.01 | 29.81 |
| | 2 | 0.03 | 6.84 | 29.81 |
| | 3 | 0.07 | 4.68 | 55.04 |

*Note.* Chirps 1, 2, and 3 correspond to low, medium, and high altitudes within the troposphere, respectively. The velocity resolution is different for one case due to different settings. "Velocity res." refers to "Doppler velocity resolution", "Unamb. velocity" refers to "Maximum unambiguous Doppler velocity", and "Range res." to "Range resolution".

impacts the precision of velocity retrievals. However, due to the narrow velocity bins (Table 1), the effect of this windowing function was limited for this study. The magnitude of this windowing ranges between 0.2 m $s^{-1}$ and 0.6 m $s^{-1}$, which is smaller than the differences in fall velocity among different hydrometeor types. More information regarding the profiler can be found by Yanovsky et al. (2023) and Unal and Brule (2024).

*Spatiotemporal matching*. First, the profiler observations were selected within the overlapping time interval of the C-band radar. Subsequently, we selected the profiler range bin closest to the midpoint of the C-band radar observation volume. This matching yielded 12 matched volumes ("points"), where the high-resolution profiler observations were aligned as closely as possible with the coarser C-band radar observations. Moreover, the profiler was matched as closely as possible to the C-band observation times for each elevation angle. To mitigate the potential influence of microscale effects on the spectra, we include three individual Doppler spectra closest to the weather radar volume and provide full vertical profiles. The greater distance of the Den Helder radar led to significantly fewer matched points, the reason why only matched observations with the Herwijnen radar were considered (Section 2.2.1).

#### 2.2.2. ARTS Scattering Database

The open-access ARTS database (Ekelund et al., 2020) contains microwave single-scattering data for 34 different types of hydrometeors. The ARTS scattering database provides scattering and extinction matrices and the absorption vector from which parameters such as single scattering albedo and back-scattering cross section can be derived (Mishchenko, 2000). The database comprises spherical liquid water droplets and ice hydrometeors ranging from pristine crystals to larger aggregates, graupel, and hail. The database was created using Mie code for spherical habits and the discrete dipole approximation method for the other shapes. Scattering properties of all hydrometeor types are available assuming random orientation, that is, for a spherically uniform probability distribution. Only two types of crystals, one aggregated and one pristine, are available in azimuthally random orientations, that is, oriented randomly in terms of the azimuthal angle but for a specific zenith orientation. When azimuthally random oriented, dual-pol variables can be derived because the asymmetry in zenith orientation allows for the separation of horizontal and vertical polarization components. For solid hydrometeors, data are provided for 35 frequencies (ranging from 1 to 886 GHz) and for temperatures of 190, 230, and 270 K. The number of temperatures might appear limited, but the impact of temperature on scattering is small (not shown). We only extracted properties corresponding to frequencies of 35 and 94 GHz corresponding to the profiler frequencies. The large plate aggregate (ID20) for snow was chosen because it was one of the two snow particle types available in a nonrandom orientation. Of the two particle types, the large plate aggregate had the most similar mass-diameter relationship to the parametrization used in HARMONIE. For graupel/hail, we selected the spherical graupel particle (ID23) for the same reason: its mass-diameter relationship most closely aligned with the parametrization used in the HARMONIE model (this model is explained in the next section). An elaborate description of the database can be found by Eriksson et al. (2018).

The liquid particles provided by ARTS were not used in this study because their scattering calculations were only performed assuming spherical drop shapes, whereas larger liquid drops are known to be more oblate due to a combination of drag forces and internal circulation (Pruppacher & Klett, 2010). Hence, we carried out T-matrix calculations (Mishchenko, 2000) to include scattering properties of oblate droplets using drop shape-diameter relationships as defined by Andsager et al. (1999). The complex refractive index of water was obtained from Liebe et al. (1991). We assumed that all raindrops are oriented horizontally, that is, the canting angles have a monodisperse distribution at 0°. We used the same three temperatures as those available in the ARTS database.

#### 2.2.3. HARMONIE-AROME Temperature and Wind

The numerical weather prediction model HARMONIE-AROME (referred to as HARMONIE in the remainder of this paper) offers high-resolution (~2.5 km) weather forecasts across Europe. Although the model comprises various atmospheric variables, only wind and dry-bulb temperature data were extracted. Wind observations were used to address aliasing in the profiler Doppler observations. Temperature data were used in the C-band attenuation correction method (Overeem et al., 2021) and as input for the HMC (Section 2.3). Moreover, the HARMONIE temperature was used to select the scattering properties from the ARTS database and the T-matrix calculations for the closest available temperature. We have not interpolated the temperatures for the scattering database due to the limited influence of temperature (Section 2.2.2). Further information about HARMONIE can be found by Bengtsson et al. (2017).

### 2.3. Hydrometeor Classification

#### 2.3.1. Description of Dual-Pol Observations

Both $Z_{\mathrm{H}}$ and $Z_{\mathrm{V}}$ from the C-band weather radar were corrected for clutter with a fuzzy logic algorithm and for rain-induced attenuation along the radar beam (Overeem et al., 2020, 2021). From $Z_{\mathrm{H}}$ and $Z_{\mathrm{V}}$, the differential reflectivity $(Z_{\mathrm{DR}})$ was derived, offering insight into the shape and orientation of hydrometeors, and, in the case of raindrops, their sizes (Kumjian, 2018; Seliga & Bringi, 1976). For instance, large raindrops result in higher $Z_{\mathrm{DR}}$ values due to their oblateness (Section 2.2.2). The copolar correlation coefficient $\left(\rho_{\mathrm{HV}}\right)$ quantifies the correlation between radar-received signals at horizontal and vertical polarizations. A high $\rho_{\mathrm{HV}}$ indicates the presence of one hydrometeor type in the radar measurement volume, such as pure snow or rain, while lower values indicate more complex scatterers (e.g., a mixture of hydrometeor types or objects larger than the wavelength). Hence, lower values are also useful for detecting nonmeteorological echoes (Chen et al., 2022; Fabry, 2015). Lastly, specific differential phase $(K_{\mathrm{DP}})$ describes the phase shift difference between horizontally and vertically polarized radar signals along the propagation path. $K_{\mathrm{DP}}$ assists in detecting intense rain rates when reflectivity is attenuated (Rauber & Nesbitt, 2018).

#### 2.3.2. Implemented HMC Scheme

HMC algorithms using dual-pol variables are available in various types (Al-Sakka et al., 2013, their Table 1) with fuzzy logic algorithms demonstrating particular effectiveness for HMC (Bringi & Chandrasekar, 2001). Therefore, we implemented the HMC scheme available from the open-source package wradlib (Heistermann et al., 2013; Mühlbauer et al., 2020). This HMC scheme uses the procedure as defined by Zrnić et al. (2001) and 2D trapezoidal membership functions based on Straka et al. (2000).

The wradlib HMC scheme uses $Z_{\mathrm{H}}$, $Z_{\mathrm{DR}}$, $\rho_{\mathrm{HV}}$, $K_{\mathrm{DP}}$ (Section. 2.3.1), and HARMONIE temperature (Section 2.2.3) through a fuzzy logic approach. Each input variable contributes to defining how strong a certain observation belongs to a specific hydrometeor type, known as "degree of membership" but referred to as "probability" in this study. Trapezoidal membership functions enhance the classification's flexibility and robustness by smoothing transitions between the 11 different types of hydrometeors considered in this algorithm. The weights for the membership functions of the four radar variables were 1, whereas the weight of the temperature membership function was 2.

In our study, we categorized the 11 hydrometeor types (with their respective group names in brackets) into four main classes: snow (dry snow, H crystals, and V crystals), rain (light rain, moderate rain, heavy rain, large drops, and rain/hail), wet snow (wet snow), and graupel (hail, rain/hail, and graupel/hail). Note that "rain/hail" is included in two classes, which is taken into account when calculating their relative probability. Wet snow was included due to its importance in preventing overestimation of mixing ratios in the melting layer. However, wet snow is not discussed in this study due to its large variability in liquid water content and the difficulty in selecting a single hydrometeor type representing wet snow from the ARTS database.

The probability of precipitation types was set to 0 if the fuzzy logic clutter algorithm classifies the range bin as nonmeteorological. All corrections and the HMC scheme were applied individually to each time step and range bin. Lastly, HARMONIE temperature data were used for postprocessing. Wet snow probability was set to 0 for temperatures below −1°C or above 7°C; rain probability was set to 0 for temperatures below −3°C; and snow probability was set to 0 for temperatures above 7°C.

### 2.4. Methodology for Comparing Profiler Observations With Theoretical Spectra From C-Band Radar Data and a Hydrometeor Classification Scheme

Observations from the profiler and C-band radar observations are not directly comparable for two reasons: first, their frequencies are different and second, Doppler data from the C-band only contain limited information about hydrometeor fall velocities because of the low elevation angles. Furthermore, the C-band radar only stores mean Doppler velocity and spectral width, whereas the profiler records full Doppler spectra for both polarizations (Section 2.2.1). To exploit all available information from the profiler, several steps are needed to simulate terminal fall velocity spectra from the C-band observations and to compare them with the profiler spectra. The full Doppler spectrum captures the variability of particle velocities within a measurement volume and provides insights into the shape of the velocity- and size-distribution of hydrometeors, hence provides beneficial information for validation of HMC schemes. The three steps required to compare the profiler and radar data are described below and illustrated in Figure 2. The implemented parametrizations are the same as those used in HARMONIE (Bengtsson et al., 2017), as we want to ultimately use the HMC output for initialization in HARMONIE.

*Step* 1 *Derivation of PSDs and fall velocities from the HMC output.* Mixing ratios ($r_i$, where $i$ represents rain, snow, wet snow, or graupel, also for the remainder of this paper) are the ratios of the mass of all hydrometeors of a given type to the mass of the volume of air containing those hydrometeors. These ratios were required to convert the scattering properties of individual particles from the ARTS database into the overall scattering characteristics for the radar's sample volume. These ratios were derived by combining C-band radar reflectivity ($Z_H$) observations with precipitation type probabilities ($P_i$) from the HMC.

To do so, we first used the reflectivity based on the PSD and assuming Rayleigh scattering for which we used:

$$Z_i = C_i \int_0^\infty n_i(D_m)\, D_V^6(D_m)\, dD_m, \tag{1}$$

where both the maximum diameter along all dimensions ($D_m$ [mm]) and the volume-equivalent diameter ($D_V$ [mm]) were used to account for irregularly shaped particles. The volume equivalent diameter represents the diameter of the liquid sphere containing the same mass of water or ice. The factor $C_i$ is necessary to account for the different hydrometeor phases and is a function of the ratio of dielectric factors:

$$C_i = F_i + (1 - F_i)\, \frac{0.177}{0.93}, \tag{2}$$

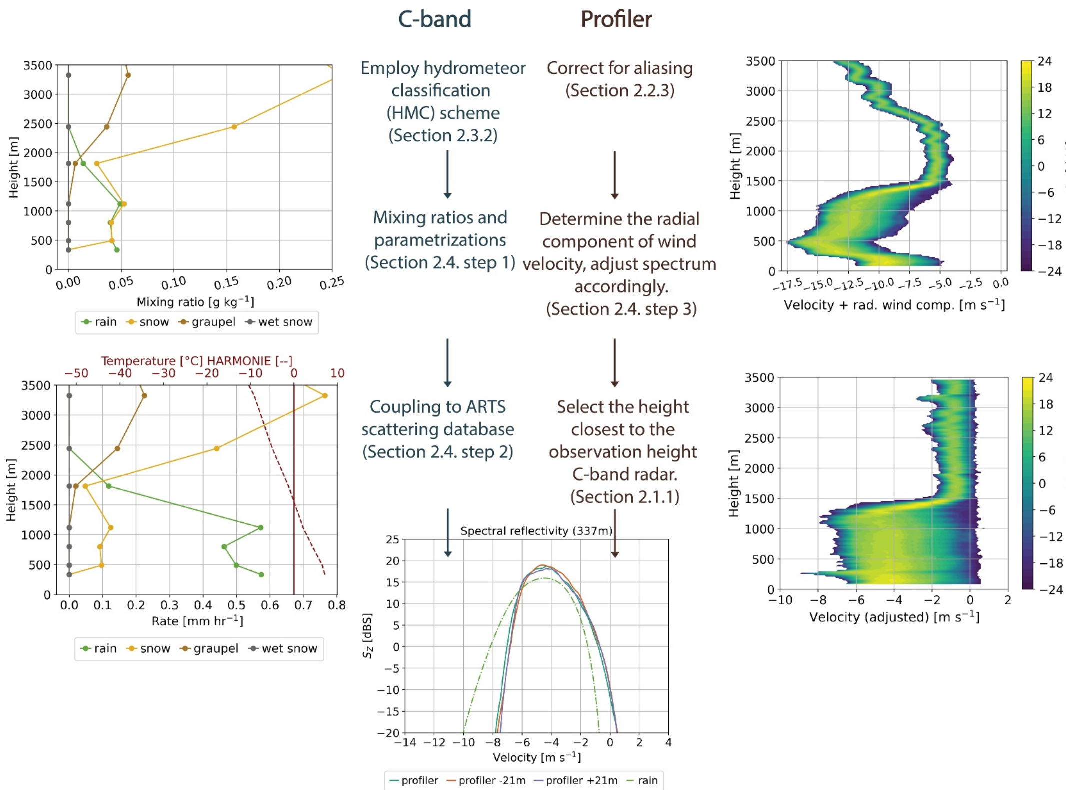


**Figure 2.** Graphical overview of Section 2, detailing the steps needed to compare the hydrometeor classification output with profiler observations. The figure indicates the subsection where each step is described. The lowest panel shows the retrieved spectra, which were used for comparison. The shown spectrogram and spectra observations are retrieved from the 35 GHz channel.

with $F$ being the fraction of liquid water as a function of hydrometeor type ($F_{\text{rain}} = 1$, $F_{\text{snow}} = F_{\text{graupel}} = 0$, and $F_{\text{wet snow}} = 0.8$). The dielectric factor of ice of 0.177 was based on the dielectric permittivity of pure ice given by Mätzler (2006). Note that the dielectric factor is nearly independent of both frequency and temperature. The value of 0.93 for the dielectric factor of water was retrieved from the C-band radar equation (Battan, 1973).

The next variable in Equation 1, $n(D_{\text{m}})$, represents the number of particles per unit volume per unit diameter ($D$), which is assumed to decline exponentially with size. The hydrometeor size distribution $n(D_{\text{m}})$ was defined as

$$n_{\text{i}}(D_{\text{m}}) = N_{0,\text{i}} \Lambda_{\text{i}}^{x_{\text{i}}+1} \exp(-\Lambda_{\text{i}} D_{\text{m}}). \tag{3}$$

Please note that Equation 3 is not a gamma distribution but is based on Caniaux et al. (1994) and Caniaux (1993). The prefactor of the exponential distribution depends on the mixing ratio through $\Lambda_{\text{i}}^{x_{\text{i}}+1}$ with $\Lambda_{\text{i}}$ (the reciprocal of the typical hydrometeor size) defined as

$$\Lambda_{\text{i}} = \left( \frac{r_{\text{i}} \rho_{\text{ref}}}{a_{\text{i}} N_{0,\text{i}} \Gamma(b_{\text{i}} + 1)} \right)^{\frac{1}{x_{\text{i}} - b_{\text{i}}}}. \tag{4}$$

In Equations 1–4, $x_{\text{i}}$ and $N_{0,\text{i}}$ are constants that vary with hydrometeor type and are defined in Table 2. The variables $a_{\text{i}}$ and $b_{\text{i}}$ are the prefactor and exponent of the mass-diameter relationship:

$$m_{\text{i}}(D_m) = a_{\text{i}} D_m^{b_{\text{i}}}. \tag{5}$$

**Table 2**
*The Constants Used in the Parameterizations for the Hydrometeor Types in This Study*

| | (Wet) snow | Graupel | Rain |
|---|---|---|---|
| $x_i$ | 1 | −0.5 | −1 |
| $N_{0,i}$ ($m^{x_i-3}$) | 5 | $5 \times 10^5$ | $8 \times 10^6$ |
| $a_i$ (kg $m^{-b_i}$) | 0.02 | 19.6 | 524 |
| $b_i$ | 1.9 | 2.8 | 3 |
| $c_i$ ($m^{1-d_i}$ $s^{-1}$) | 5.1 | 124 | 842 |
| $d_i$ | 0.27 | 0.66 | 0.8 |

The employed values of $N_{0,i}$ (based on Caniaux, 1993; Pruppacher & Klett, 2010), $a_i$, and $b_i$ (based on Locatelli & Hobbs, 1974) are given in Table 2. The reference density using a standard atmosphere ($\rho_{ref}$ [kg m$^{-3}$]) was defined as

$$\rho_{ref} = \rho_0 e^{-Lh}, \tag{6}$$

with $\rho_0 = 1.225$ kg m$^{-3}$, $h$ the height above sea level [m], and the density lapse rate $L = 1.26 \times 10^{-4}$ m$^{-1}$.

The diameters $D_V$ and $D_m$ (Equation 1) can be related using the following expression:

$$D_V = D_m \left(\frac{\rho_{m,i}}{\rho_{v,i}}\right)^{\frac{1}{3}}, \tag{7}$$

where $\rho_{v,i}$ [kg m$^{-3}$] is the density of purely liquid or solid water, $\rho_{m,i}$ [kg m$^{-3}$] the density of the hydrometeor, defined as its mass divided by the volume of the smallest sphere that can fully enclose it:

$$\rho_{m,i} = \frac{6a_i}{\pi} D_m^{b_i - 3}, \tag{8}$$

and $\rho_{v,rain} = 1{,}000$ kg m$^{-3}$, $\rho_{v,snow} = \rho_{v,graupel} = 917$ kg m$^{-3}$, and $\rho_{v,wet\ snow}$ as

$$\rho_{v,wet\ snow} = \rho_{v,snow} + F_{wet\ snow}(\rho_{v,rain} - \rho_{v,snow}). \tag{9}$$

Substituting Equation 7 in Equation 1 yields:

$$Z_i = C_i \int_0^\infty n_i(D_m) \left(\frac{\rho_{m,i}}{\rho_{v,i}}\right)^2 D_m^6 dD_m. \tag{10}$$

Finally, as $\Lambda$ depends on the mixing ratio according to Equation 4, Equation 10 can be reformulated to express $r_i$ as a function of $Z_i$:

$$r_i = A_i Z_i^{B_i}, \tag{11}$$

with

$$B_i = \frac{x_i - b_i}{x_i - 2b_i}, \tag{12}$$

and

$$A_i = \frac{a_i N_{0,i} \Gamma(b_i + 1)}{\rho_{ref}} \left( \frac{1}{C_i \left(\frac{6a_i}{\pi \rho_{v,i}}\right)^2 N_{0,i} \Gamma(2b_i + 1)} \right)^{B_i}. \tag{13}$$

To link the HMC output to physical precipitation characteristics, we assumed that the ratio of the mixing ratios was equal to the ratio of the probabilities:

$$\frac{r_i}{r_j} = \frac{P_i}{P_j}, \tag{14}$$

and by definition:

$$Z = \sum_i Z_i, \tag{15}$$

with $Z$ representing the (total) reflectivity as measured by a radar. Combining Equations 11, 14 and 15 yields a system of equations from which the mixing ratios of all hydrometeor types can be solved numerically. An example for snow is provided in Appendix A.

Finally, to convert the diameters to terminal fall velocity, the following relation was used:

$$v_f(D_m) = \left(\frac{\rho_0}{\rho_{ref}}\right)^{0.4} c_i D_m^{d_i}, \tag{16}$$

where $c_i$ and $d_i$ are constants that vary with hydrometeor type and are defined in Table 2. The parameters for rain were based on Foote and du Toit (1969) and Liu and Orville (1969), parameters for (wet) snow and graupel were set as by Engdahl et al. (2020).

Precipitation rates for the different hydrometeor types are expressed as

$$R_i = \int_0^\infty n_i(D_m) \frac{\rho_{m,i}}{\rho_{v,i}} D_m^3 v_f(D_m)\, dD_m, \tag{17}$$

resulting in a power-law relationship between mixing ratio and precipitation rate. This is similar to the relationship between mixing ratio and reflectivity (Equation 11).

*Step* 2 *Couple PSDs with the scattering database.* The HMC output provides the probabilities of various hydrometeor types within a given measurement volume. In case of snow and graupel, these were selected from the ARTS database. From the 34 hydrometeor types available in the ARTS database, we chose those with mass-diameter relationships similar to the HARMONIE relationships for consistency. In the case of rain, the hydrometeor scattering properties were derived using the T-matrix method.

The individual scattering properties from either the T-matrix calculations or the scattering database are combined with the retrieved PSDs to calculate spectra $S_Z$ [$\mathrm{mm^6 m^{-3} (m\ s^{-1})^{-1}}$] that could be compared to those retrieved from the profiler:

$$S_{ZH}(v_f) = z_H(D_m(v_f))\, n(D_m(v_f)) \frac{\mathrm{d}D_m}{\mathrm{d}v_f}, \tag{18}$$

with $z_H(D_m)$ the contribution of a single particle with diameter $D_m$ to the horizontal reflectivity. Note that Equation 18 does not account for broadening caused by factors such as horizontal wind variations and turbulence within the radar sampling volume. Spectral differential reflectivity was defined as

$$S_{DR} = \frac{S_{ZH}}{S_{ZV}}, \tag{19}$$

and the dual wavelength ratio (DWR) as

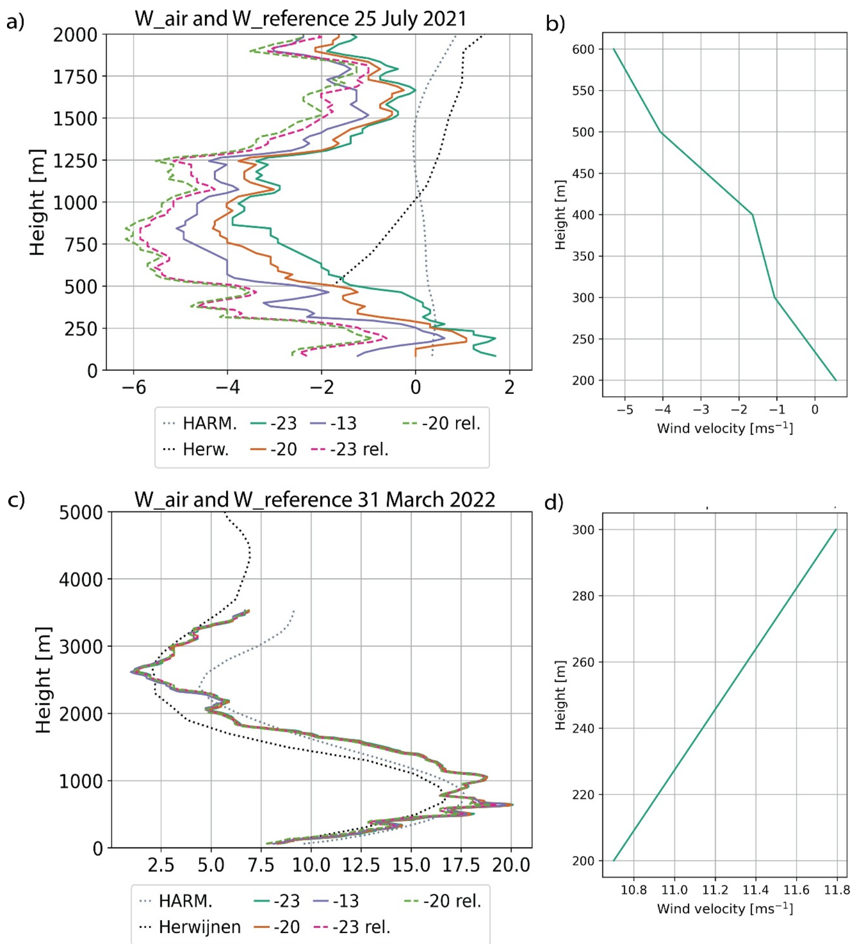


**Figure 3.** (a) Simulated $W_{\mathrm{air}}$ values for a convective event on 25 July 2021. The values were derived using various thresholds: solid lines represent absolute thresholds, and dashed lines represent thresholds that include total reflectivity ("relative"), all in dB$S$. The dotted lines indicate radial wind components from HARMONIE model output and from wind profiles extracted from the Herwijnen radar (Holleman, 2005) (b) Example of lidar data for the same date as panel (a). No signal was detected above 600 m. (c) Same as panel (a) but for 31 March 2022, a stratiform case with embedded convection and snowfall. (d) Same as panel (b) but for 31 March 2022. Note that the $y$-axes are different for each subfigure.

$$S_{\mathrm{DWR}} = \frac{S_{Z35}}{S_{Z94}}, \tag{20}$$

with $S_{Z35}$ the spectral (horizontal) reflectivity at 35 GHz and $S_{Z94}$ the spectral (horizontal) reflectivity at 94 GHz. To account for the different velocity resolutions of the 35 and 94 GHz channels (Table 1), observations are first interpolated onto uniformly spaced bins of 0.1 m s$^{-1}$ followed by the calculation of the DWR. In the results section, we present spectra on a logarithmic scale [dB$S$].

*Step* 3 *Retrieval of spectra from profiler.* The profiler, operating at a 45° elevation angle, captures both Doppler velocities and dual-pol variables, providing extensive data on hydrometeor properties. A drawback of this elevation angle is that Doppler velocities reflect both hydrometeor terminal fall velocity and horizontal wind (right upper panel Figure 2). To remove the radial wind component, we assume the smallest particles have zero fall velocity and use them as passive tracers (Williams et al., 2000). For this, we used either fixed or relative thresholds. The fixed threshold sets a minimum absolute reflectivity intensity that must be exceeded to represent the smallest particles, whereas the relative threshold was normalized by the total reflectivity. In case of the relative threshold, the total reflectivity for a specific range bin and time step is calculated first. This value (expressed in dB$Z$) is then added to the constant threshold (e.g., −20 dB$S$). This dynamic adjustment creates a threshold that can account for variations in reflectivity, such as the differences between the smallest snow particles and the smallest raindrops. Then, for both the relative and absolute thresholds, the threshold must be exceeded in a specified number of adjacent Doppler velocity bins (various values were tested). The highest velocity (note that velocities toward the radar are negative) at which this occurs was used as the radial wind component, referred to as $W_{air}$. The determination of $W_{air}$ was based on 35 GHz channel observations and applied to both the 35 and 94 GHz observations. We evaluated this assumption and tested its sensitivity to certain thresholds using C-band radar (Herwijnen) wind estimates and HARMONIE wind output (example shown in Figure 3). Additionally, we tried implementing simultaneous observations from a Windcube 200S scanning Doppler wind lidar also located in Cabauw. More details regarding this instrument can be found by Dias Neto et al. (2023). However, this data was constrained to the lower atmosphere due to the lidar's sensitivity to rainfall (Figures 3b and 3d). Hence, the lidar was not used in the remainder of this study.

Sensitivity to the choice of threshold was found to depend on the precipitation type. The threshold yielded varying results especially during the convective case (Figure 3a) when hydrometeors are larger. To maintain consistency, we used a fixed threshold of −20 dB$S$ for all cases in Section 3. Other $W_{air}$ values are included in the figures to assess the sensitivity of $W_{air}$ on the threshold. A more detailed investigation into this issue is beyond the scope of the current analysis.

Additionally, we implemented the DWR using the profiler's dual-frequency capability. The DWR can be used to identify the "Mie notch" (Kollias et al., 2002), which arises due to variations in scattering behavior at different frequencies for particles of the same size. A particle exits the Rayleigh regime and enters the Mie regime when its size increases to a value comparable to the wavelength corresponding to the employed radar frequency. For instance, a particle with a size similar to the wavelength of a 94 GHz radar (3.2 mm) will exhibit Mie scattering, whereas the same particle may still exhibit Rayleigh scattering at 35 GHz (8.6 mm wavelength). The Mie notch is identified by a significant change in scattering behavior when comparing signals at these two frequencies and is calculated as the ratio of reflectivities (we used the horizontal reflectivity) from the 35 GHz to the 94 GHz channel. Since the theoretical location of the first maximum is known, the difference between the simulated and observed Mie notch can be used to estimate wind velocity. Subsequently, this difference can be used to derive the radial component of the wind velocity.

## 3. Results

Six cases were selected for analysis. The first three are "simple" cases involving stratiform rain with low intensities near the Earth's surface. The fourth case involves high-intensity convective rain. Lastly, two cases of snow at the surface were chosen. These cases represent a range of midlatitudinal common weather conditions, allowing us to demonstrate our method across the most frequently occurring precipitation types. Each case is discussed separately using the spectrogram of that certain event, the output from the HMC scheme and spectra at a selected height, all based on the 35 GHz channel. Values below −20 dB$S$ are masked to remove noise from spectra at a selected height.

### 3.1. 3 February 2021, Low Intensity Precipitation on a Winter Day

The first case study involves light precipitation intensities (Figures 4a and 4b). In the upper atmosphere, precipitation is solid due to the freezing temperatures. The temperature increases toward the Earth's surface and the height of the zero-degree isotherm (around 1,500 m) aligns with an increase in fall velocities and increase in reflectivity (Figure 4c). Both increases are expected: the rise in fall velocity, since snowflakes have lower terminal fall velocities than raindrops that are expected below the zero-degree isotherm and the rise in reflectivity due to the bright band. Even though the melting layer is clearly visible starting at around 1,500 m, the HMC algorithm indicates a 50% chance of snow, although the converted snow rate is low.

The smallest particles are used as passive tracers to adjust for wind velocity (Section 2.4) in the spectrogram (Figure 4c). The validity of this assumption can be assessed by analyzing the presence of a Mie notch in the DWR, which is particularly pronounced for raindrops (Section 2.4). This analysis identifies the threshold incorporating relative reflectivity ("rel") as the best fit (Figure 4d). The fixed threshold at −20 dB$S$ (used to adjust the spectrogram shown in Figure 4c and spectra in Figure 4e) provides reasonable results as well, as the shapes of the observed and simulated spectra are similar. However, removing the radial wind component using the fixed threshold results in an underestimation of the fall velocities, visible as a slight rightward shift in Figure 4e. Lastly,

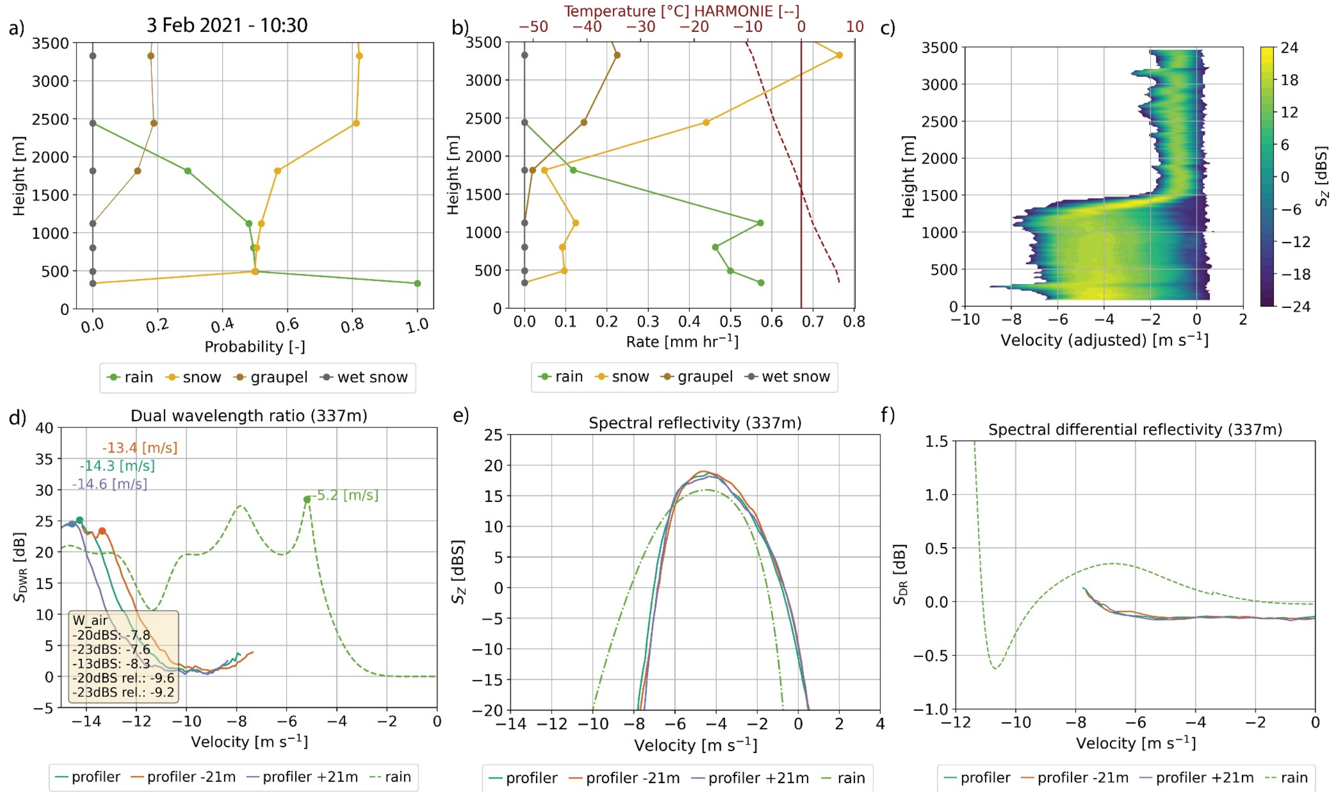


**Figure 4.** Precipitation characteristics on 3 February 2021 at 10:30 (UTC): (a) Probabilities of four hydrometeor types based on the wradlib hydrometeor classification (HMC) scheme. (b) Precipitation rates based on the HMC probabilities and derived mixing ratios. Temperature (red) is retrieved from the HARMONIE model (dashed). (c) Spectrogram from profiler observations at one time step (10:30). Velocity ($x$-axis) adjusted for the wind component assuming the smallest particles behave as passive tracers. (d) Observed (solid) and simulated (dashed) $S_{\mathrm{DWR}}$ (based on the ratio of $Z_{H35}$ and $Z_{H94}$) at 337 m. The three solid lines represent the profiler observations most closely to that of the C-band radar ("profiler") and 21 m below ("profiler −21 m") or above ("profiler +21 m"). The measured $S_{\mathrm{DWR}}$ is dealiased, but, as opposed to the other panels in this figure, is not corrected for $W_{\mathrm{air}}$ (e) Observed (solid) and simulated (dashed) spectra at 337 m, one particular height from the spectrogram shown in panel (c). (f) Observed (solid) and simulated (dashed) $S_{\mathrm{DR}}$ at 337 m. Note that in the entire study negative velocities indicate direction toward the surface. The observed spectra in (e) and (f) have been adjusted to account for wind influence ($W_{\mathrm{air}}$). The presented spectrogram, spectra, and spectral differential reflectivity of all figures in this manuscript are obtained from the 35 GHz channel and all values below −20 dB$S$ are masked to remove noise.

$S_{\mathrm{DR}}$ is expected to increase for larger raindrops as their oblateness increases (Figure 4f). The first bump shows a slight displacement of around $-2$ m s$^{-1}$ similar to the difference in shift between the Mie notch and the fixed threshold used to remove the radial wind component. The increase in simulated $S_{\mathrm{DR}}$ between $-2$ m s$^{-1}$ and $-6$ m s$^{-1}$ is absent in the observed spectra. The constant negative signal is most likely related to calibration offsets. The increase in $S_{\mathrm{DR}}$ observed below $-6$ m s$^{-1}$ cannot be attributed to noise because we only display the spectrogram if both underlying signals are well above the noise. The deviations between the observed data and the theoretical curve can be attributed to several factors. These include the adopted size-shape relationship (we use that of Andsager et al., 1999), the distribution of canting angles (the theoretical curve assumes a canting angle of 0°), and a combination of uncertainties arising from the velocity axis shift and the assumed size-velocity relationship.

In addition to the clear and expected $S_{\mathrm{DWR}}$ signatures in the signal, such as the sharp increase from $-11$ m s$^{-1}$ onward and the sudden bump between $-14.5$ and $-13$ m s$^{-1}$, referred to as the Mie notch, we also observed more unexpected behavior, such as the 5 dB increase for the smallest particles, which remains unexplained at this time.

### 3.2. 29 April 2021, Low-Intensity Precipitation on a Spring Day

The spectrogram on 29 April 2021 (Figure 5c) is similar to the previous case (Figure 4c), though fall velocities are higher in the April case. Although it is an unusually cold spring day, snow is not reported on the ground. However, the HMC output indicates high probabilities of snowfall near 50% at approximately 500 m altitude (Figure 5a).

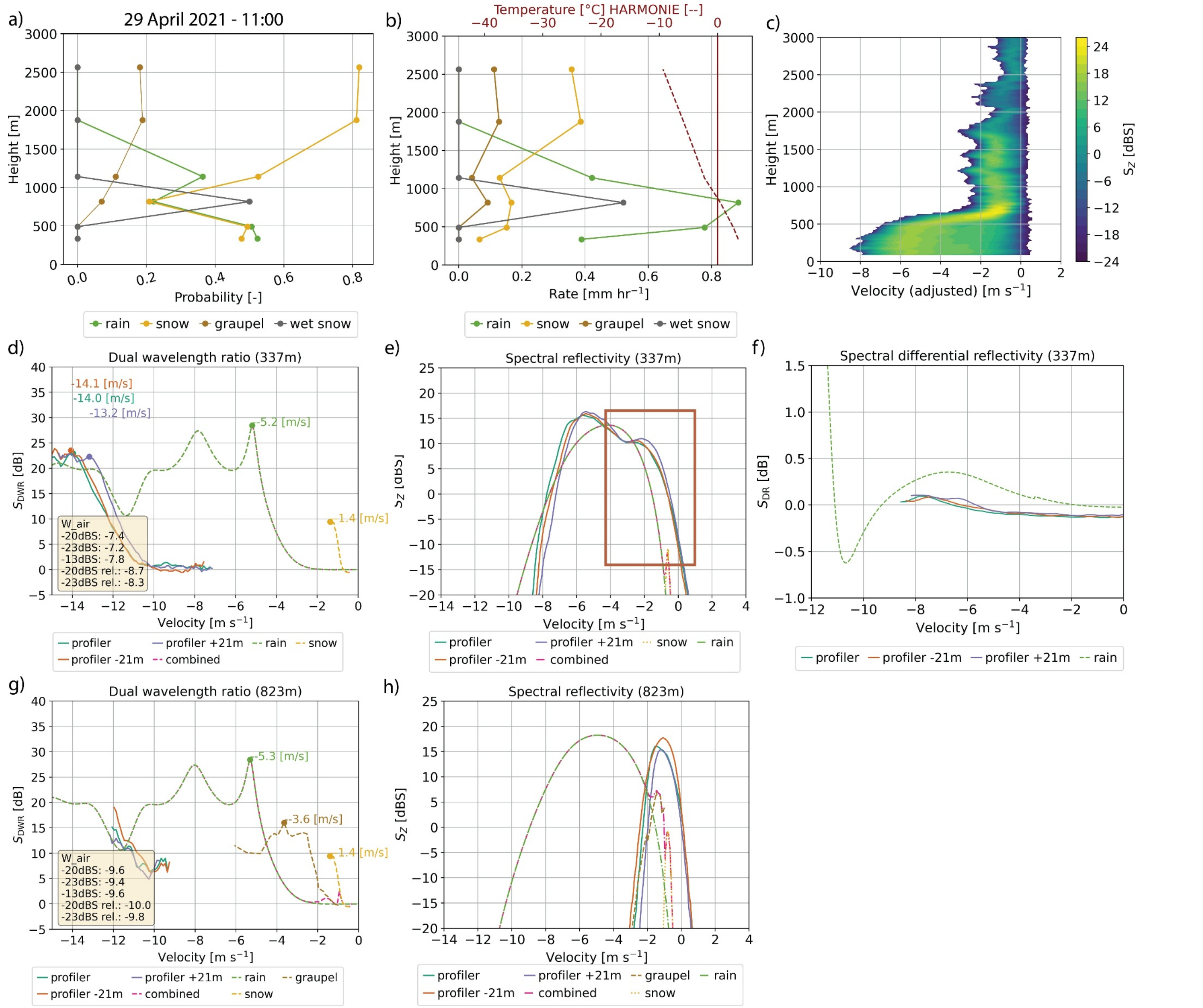


**Figure 5.** Same as Figure 4 but for 29 April 2021 and two additional panels: (g) is similar to panel (d), but for 823 m and (h) is similar to panel (e), but for 823 m. "Combined" represents the total reflectivity from the simulated spectra, combining rain, snow, and graupel. If only one hydrometeor type is present, the "combined" value corresponds directly to the reflectivity of that single type.

The first reflectivity peak is visible around $-2$ m s$^{-1}$ (Figure 5e), and another peak is visible at higher fall velocities (around $-6$ m s$^{-1}$). The second peak is related to rain, but there are several possible explanations for the first peak. The first explanation is the presence of snow particles, which is unlikely because 337 m seems well below the melting layer. A second explanation is the presence of a multi-modal rain PSD with a drizzle mode at low velocities and a rain mode at higher velocities.

To remove the radial wind component, the relative threshold ($-23$ dB$Z$ rel) again matches best if the first peak of the simulated Mie notch is used as validation. The fixed threshold at $-20$ dB$S$ results in a small shift, evident in Figures 5c and 5e. Low rain rates are associated with low $S_{DR}$ values, as smaller drops are nearly spherical. The $S_{DR}$ from the profiler increases with fall velocity, indicating that faster-falling, larger particles are more oblate (Figure 5f). However, it is important to stress that these values are associated with very low reflectivity values (Figure 5e). The limited occurrence of large particles is expected in relation with the low rainfall intensity (Figure 5b). When analyzing the spectra at 823 m (Figure 5h), the observed spectra are smaller and concentrated

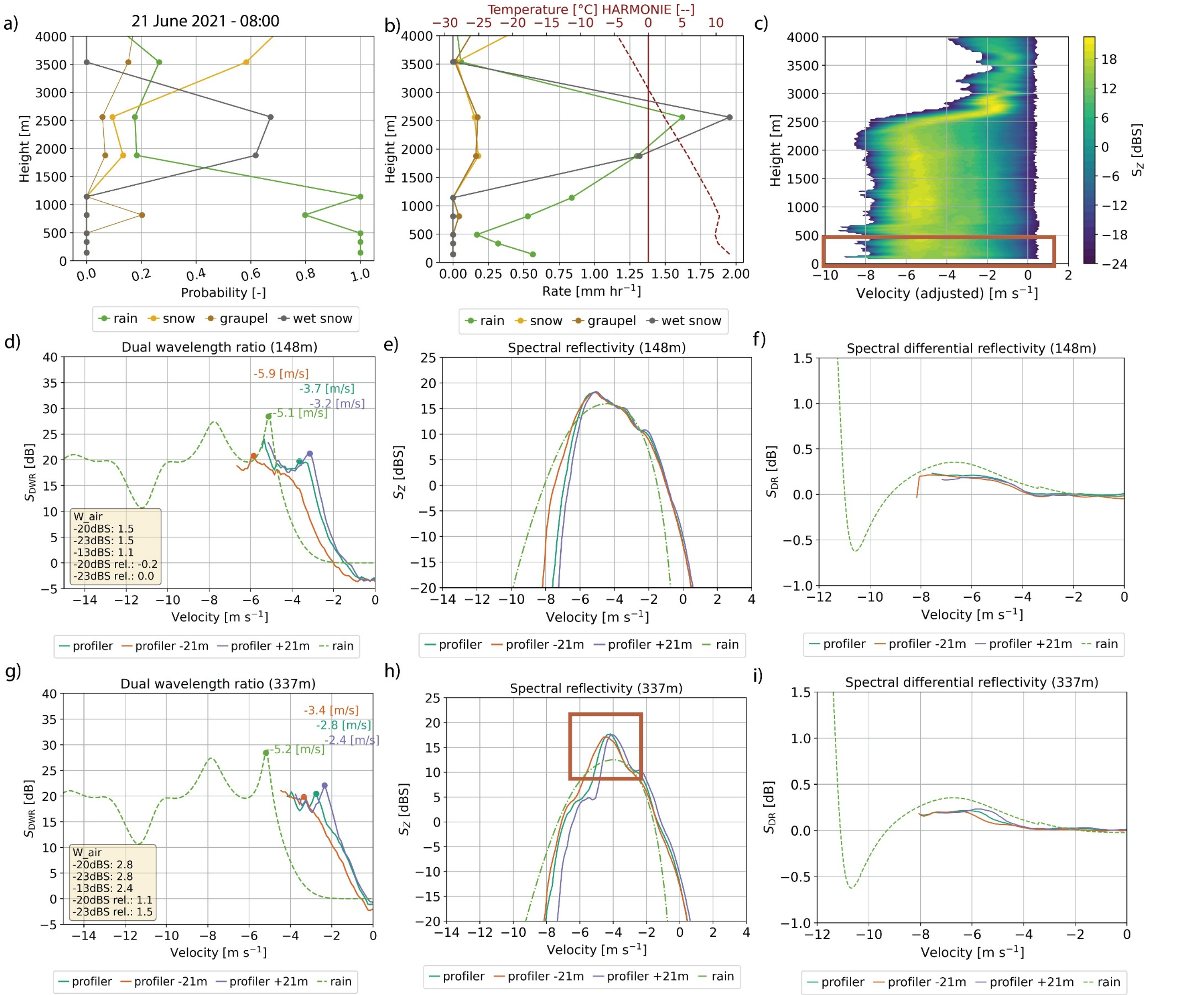


**Figure 6.** Same as Figure 4 but for 21 June 2021 and three additional panels: (g) is similar to panel (d), but for 337 m, (h) is similar to panel (e), but for 337 m, (i) is similar to panel (f), but for 337 m.

around lower fall velocities as expected for snow. Furthermore, the distinct Mie notch associated with raindrops is absent in the observed spectra (Figure 5g). Hence, the HMC falsely reports rain at 823 m.

Due to the variability in water content and shape of wet snow, accurately representing its scattering properties is complicated and outside the scope of this study. As a consequence, however, we cannot confirm the presence of wet snow or graupel. The observed reflectivity values match those of the simulated raindrops (peak value around 17–18 dBZ, Figure 5h, green dashed line), whereas the relatively narrow shape of the spectra and low fall velocities resemble that of snow (Figure 5h, dotted yellow line). Graupel is reported to exhibit weaker backscattering than the observed values (Garrett et al., 2012) and the simulated shape of the graupel spectra also differs from that of the observed spectra (Figure 5h, dashed pink line). This in combination with the observed terminal fall velocities in the wet snow range (Yuter et al., 2006) and the temperature slightly above the freezing level favor the presence of the latter.

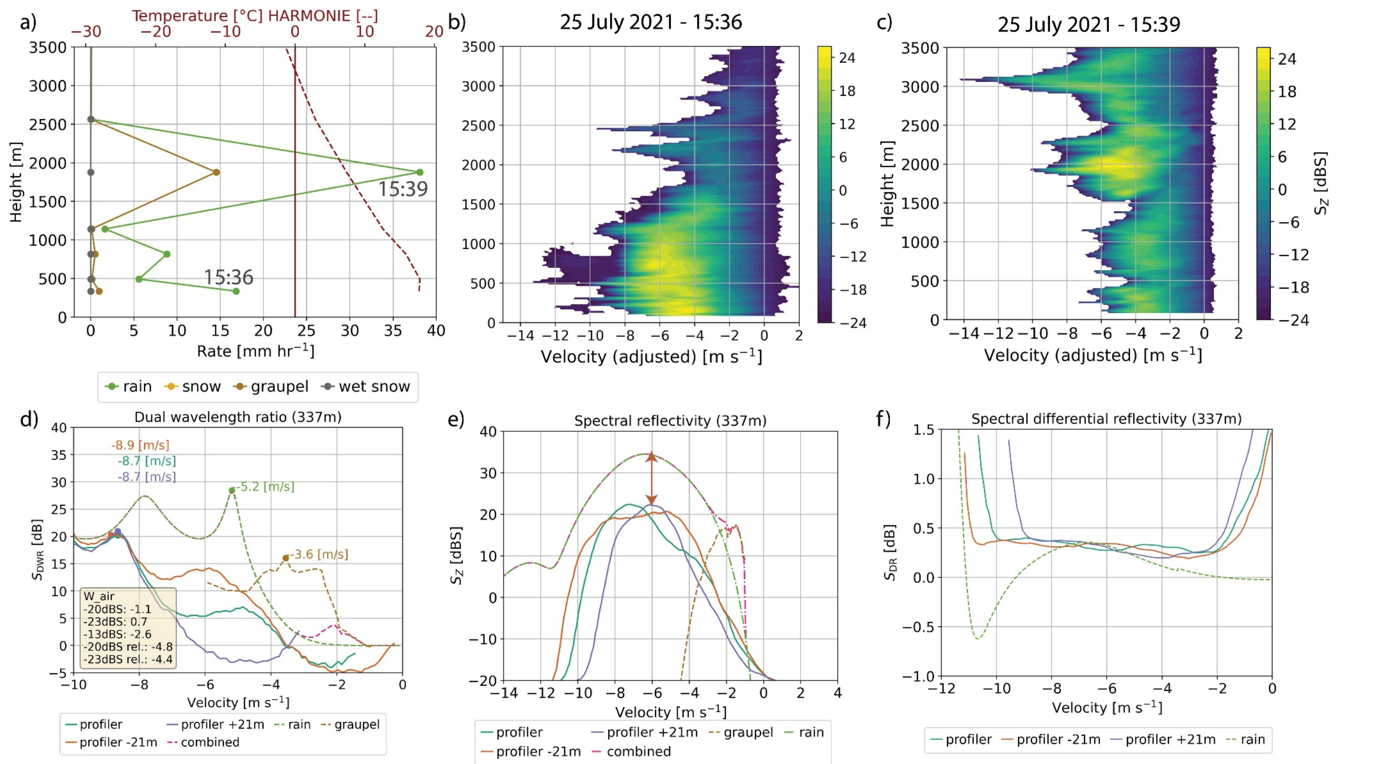


**Figure 7.** Same as Figure 4 but for 25 July 2021. Additionally, the rain rates and temperature in panel (b) are replaced with a spectrogram similar to that in panel (c). The lower panels all correspond to observations made at 15:36.

### 3.3. 21 June 2021, Low Intensity Rain on a Summer Day

The zero-degree isotherm for another "simple" rain case, occurring at 21 June 2021, is higher than the previously discussed cases (Figures 4b and 5b) and is above 2,000 m (Figure 6b). As a consequence, the melting layer is also higher and is located between 2,600 and 3,000 m (Figure 6c). Below the melting layer, the reflectivity values are lower, indicating the hydrometeors are fully melted. This is in agreement with the high probability of rain according to the HMC scheme especially below 1,100 m. To remove the radial wind component, which is minimal for this case, the result using the fixed threshold at −20 dB*S* aligns best with the shift of the Mie notch. Despite a small shift, the shapes of the simulated (Figure 6e, dashed) and observed spectra (Figure 6e, solid) are very similar. The minor bump visible around −6 m s$^{-1}$ corresponds with the small peak visible at the lowest part of the adjusted spectrogram (Figure 6c). The bump is even more apparent at 337 m (Figure 6h, around −4 m s$^{-1}$, especially the "+21 m" observation). At the same height, a small peak in the $S_{\mathrm{DWR}}$ is visible (Figure 6g, around −2 m s$^{-1}$). The observed spectral reflectivity exhibits variability in the raindrop size distribution that is not represented in the model. However, the spectral differential reflectivity maintains a similar shape to the modeled values. Due to the influence of the canting angle distribution (Unal & Brule, 2024), the measured $S_{\mathrm{DR}}$ values are slightly lower than those predicted by the model.

### 3.4. 25 July 2021, Convective Rainfall

25 July 2021 was a day with very high precipitation intensities in the Netherlands, which even resulted in flooding. Unlike the previous rain cases, the rain of this day is associated with high precipitation rates and is considered "convective", confirmed by the absence of a (consistent) melting layer visible near the zero-degree isotherm (Figures 7a–7c). As a consequence, accurate time matching is crucial as convective events vary strongly in both space and time. This is demonstrated in Figures 7a–7c: the lowest scan elevation of the C-band radar at 15:36 shows intense rainfall rates (Figure 7a), corresponding to the peak visible below ~1,000 m in Figure 7b, whereas three minutes later the high reflectivities below 1,000 m have disappeared. A new peak appears higher up in the atmosphere, around 2,000 m (Figure 7c), corresponding to the 15:39 scan. Note that this

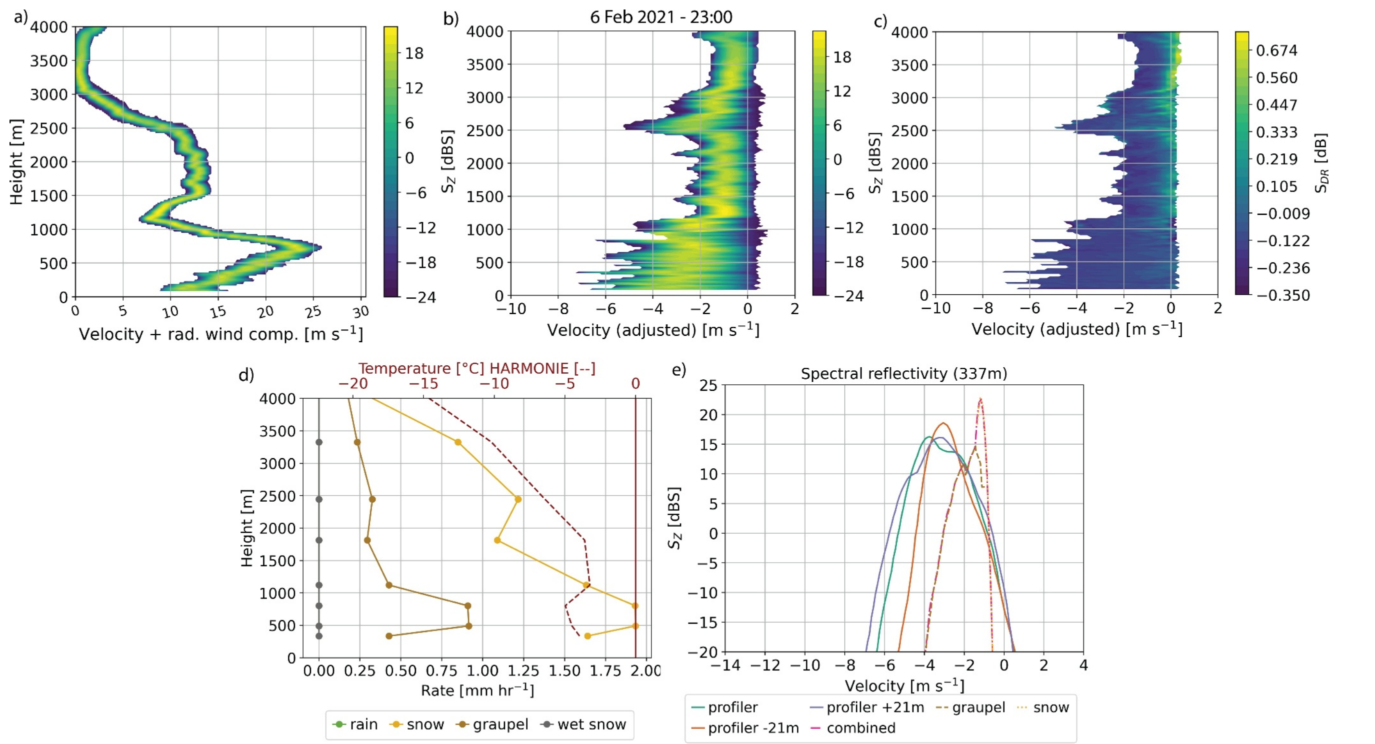


**Figure 8.** Precipitation characteristics on 6 February 2021 at 23:00 (UTC): (a) Dealiased velocity as observed by the profiler (radial wind component not removed). (b) Spectrogram after removing the radial wind component assuming the smallest particles behave as passive tracers. (c) Same as (b), but for the differential reflectivity. (d) Precipitation rates based on the hydrometeor classification probabilities and derived mixing ratios. Temperature (red) is derived from the HARMONIE model. (e) Observed (solid) and simulated (dashed) spectra at 337 m. "Combined" represents the total reflectivity from the simulated spectra, combining rain, snow, and graupel.

is not only related to vertical variation in the storm but also to horizontal variability, as the profiler measures at a 45° elevation angle. The profile measured at 15:39 also shows a peak with large vertical velocities at the zero-degree isotherm, around 3,000 m, indicating the presence of graupel or hail particles. Another difference with the previous cases is that the profiler suffers from severe attenuation, resulting in reflectivity values more than 10 dB*Z* lower than the reflectivity values observed by the C-band radar (Figure 7e, indicated by the vertical orange arrow). The discrepancies in the simulated and observed spectra at higher terminal fall velocities are likely related to the simple fall speed relation used to simulate raindrops.

The large variability in this case is also visible when we only focus on the observed spectra (Figures 7d and 7e). Despite their close proximity, all within 100 m, they are different: the two closest to the surface, "profiler −21 m" and "profiler", show an additional bump in the $S_{DWR}$ around $-6$ m s$^{-1}$ and $-5$ m s$^{-1}$, respectively (Figure 7d). The first bump, smaller than the one associated with raindrops around $-8.7$ m s$^{-1}$, suggests that the presence of an additional precipitation type. Strong convection favors the presence of graupel or hail, which is indicated by the HMC output as well (Figure 7a). The observed $S_{DR}$ values do not vary as much with fall velocity as one would expect in case of pure rain (Figure 7f). The constant $S_{DR}$ at fall velocities between $-9$ m s$^{-1}$ and $-4$ m s$^{-1}$ might be indicative of the presence of graupel or hail. Because these hydrometeors tumble, they lack the distinct orientation that larger raindrops have, resulting in low constant $S_{DR}$. The fact that the observed $S_{DR}$ has a relatively high constant value is likely a result of a calibration offset.

Furthermore, higher spectral differential reflectivity values occur at low ($v \geq -2$ m s$^{-1}$) and high ($v \leq -8$ m s$^{-1}$) fall velocities. At low velocities, this could be indicative of the presence of small ice particles. At high velocities, the increase could be due to the Mie effects also present in the theoretical differential reflectivity spectrum for rain. The measured spectra do not exhibit the clear dip associated with Mie scattering. This may be explained by the smearing effect that turbulence and the presence of possibly three PSDs (small ice particles, graupel/hail, and rain) can have.

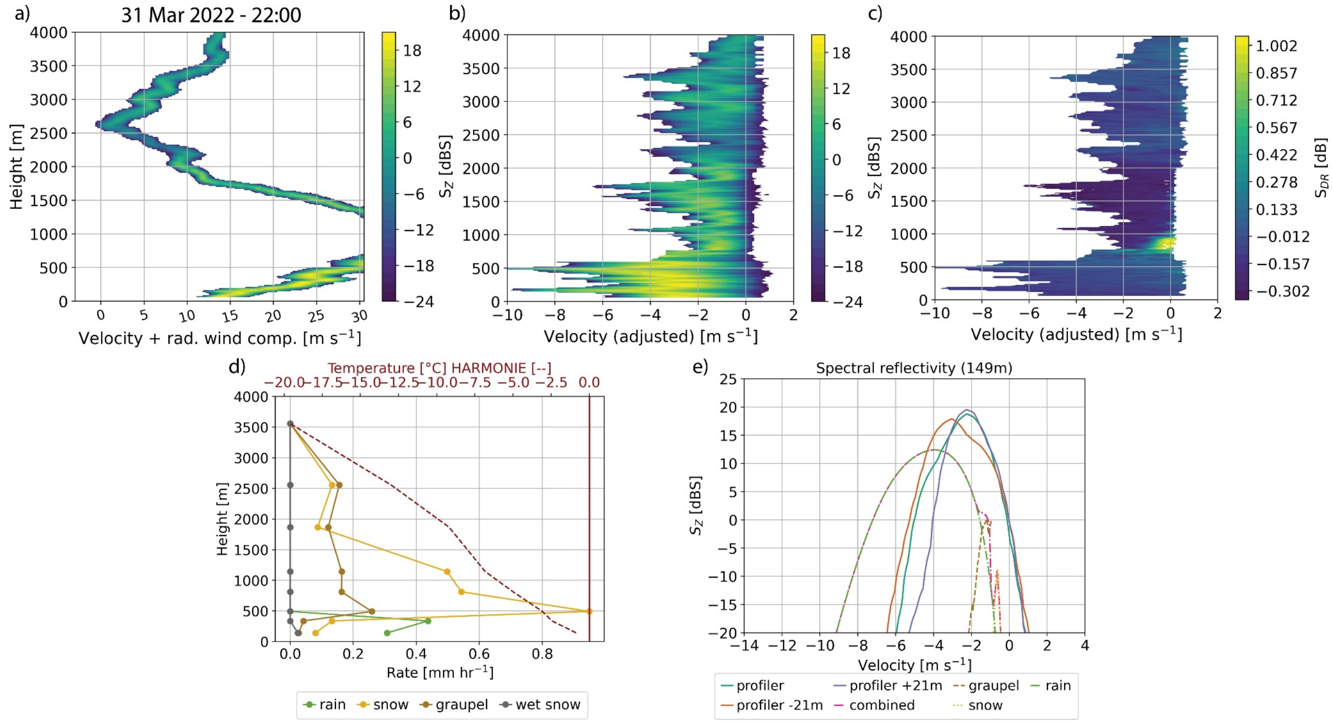


**Figure 9.** Same as Figure 8 but for 31 March 2022.

The variation between the differential reflectivity spectra (Figure 7f) at the three heights (±21 m) coincides with the Mie notches in Figure 7d, which could indicate that the $w_{air}$ estimates are associated with large uncertainties.

### 3.5. 6 February 2021, Snowstorm "Darcy"

The last two cases involve snowfall at the ground. The first occurred on the evening of 6 February 2021, for which a weather warning was issued due to icy conditions. The unadjusted spectral reflectivity profile (Figure 8a) reveals significant variability in measured velocity, which can be attributed to the influence of wind velocity on profiler observations. Strong wind particularly affects snow, as these particles have a low inertia. Our method does not account for variation in wind within one bin and this likely causes the horizontal fluctuations in the adjusted spectrogram (Figure 8b) and broadened spectra (Figure 8e). For snow, low fall velocities are expected (simulated by dashed lines) but the actual spectra from the profiler (solid lines) are broader and associated with higher fall velocities. When focusing at the vertical area between 1,500 and 2,000 m where wind velocity seems stable (Figure 8a), the range of fall velocities is reduced between $-3.5$ m s$^{-1}$ and 0 m s$^{-1}$ (Figure 8b). Still, the fall velocities are higher than expected, indicating the presence of graupel or hail. The presence of graupel or hail is suggested by the HMC scheme (Figure 8d) and the width of the observed spectra overlaps with the simulated fall velocities (Figure 8e). Broader spectra are indicative of strong turbulence, which is likely in this case. Moreover, the individual contributions of simulated snow and graupel are too low, whereas the peak of the combined spectrum is closer to the observed peaks, even slightly higher. $S_{DR}$ exhibits elevated values at heights corresponding to the expected dendritic growth layer, with the $-10$°C isotherm located at approximately 3,000 m (Figure 8c). The high $S_{DR}$ values, indicating oblate particles, are associated with low fall speeds, indicating a high probability of dendrites. From 1,000 m and below $S_{DR}$ becomes rather flat, which corresponds to snow and spherical graupel in a turbulent medium.

### 3.6. 31 March 2022, Snow in Spring

The second snowfall case at the ground, on the evening of 31 March 2022, is also accompanied by high wind velocities (Figure 9a). Unlike the previous case, the temperature was close to 0°C near the ground. Melting particles result in increased reflectivity values as visible in the lowest 600 m of the atmosphere (Figure 9b). Furthermore, the HMC indicates the possibility of rain for this event. As a consequence, a broadening of the spectra (Figure 9e) compared to the previous case (Figure 8e) should be visible. However, both spectra exhibit similar widths, which can be attributed to either wind variability within a single bin or the presence of rain. When using the smallest particles as passive tracers, we are unable to distinguish between these two causes of spectral broadening. When solely focusing on the three observed spectra, the one closer to the surface (profiler −21 m, orange line, Figure 9d) shows an increase in reflectivity around −3 m $s^{-1}$. These velocities are more representative for wet snow than for rain. The $S_{DR}$ profile (Figure 9c) exhibits a relatively uniform signature below 700 m likely associated with a mixture of snow, wet snow, and small raindrops. Notably, the elevated $S_{DR}$ values at low fall velocities between approximately 700 and 900 m, in conjunction with the temperature range, suggest the potential presence of columnar ice crystals.

## 4. Discussion

This study explores the potential of a dual-polarization, dual-frequency profiler at a 45° elevation angle to evaluate the performance of an HMC scheme. This study is exploratory in nature and therefore aimed at examining the potential opportunities and challenges associated with the use of a slanted profiler. Given the limited amount of research on this topic (Mak & Unal, 2025; Unal & Brule, 2024), the objective was to provide an overview of the challenges associated with these measurements. These points can be addressed in detail in future research. The profiler that we use can clearly show two characteristics of the melting layer in one measurement (Figure 4c–6c): a sudden increase in velocity (Baldini & Gorgucci, 2006) and reflectivity (Fabry & Zawadzki, 1995; Hall et al., 2015; Harrison et al., 2000). Additionally, on 25 July (Figure 7), the combination of high terminal fall velocities and $S_{DR}$ values indicates intense rainfall with oblate and large raindrops (Andsager et al., 1999; Zheng et al., 2023). We also show that snow velocities, when not affected by convective motions or turbulence (Figure 8e), are low (Garrett et al., 2012; Zawadzki et al., 2010) and do not show a very clear peak in the $S_{DWR}$ when the liquid water content is low (Karrer et al., 2022). Lastly, our findings demonstrate that raindrop fall velocities can be distinguished from radial wind using the Mie notch (Kollias et al., 2002; Tridon & Battaglia, 2015). Although not the main aim of this study, we also present a method to estimate mixing ratios from HMC output and corresponding reflectivities. Accurate mixing ratios are essential to initialize weather forecast models due to their influence on cloud formation (Gao & Li, 2008) and the likelihood and intensity of precipitation (Argence et al., 2008; Hong et al., 2004) and can be used to initialize 3D precipitation fields in weather models, thereby enhancing precipitation forecasts.

The HMC output occasionally produces results that, at a first glance, seem unrealistic in comparison to profiler observations, such as showing a high probability of snow near the Earth's surface in Figure 4a. These results underscore the value of vertical profiles in assessing HMC schemes and emphasize the need for further evaluation of the algorithm, such as exploring the outcomes of the member functions in this case. Identifying the origin of the discrepancies between observed and simulated spectra appeared to be difficult as multiple assumptions are required to simulate spectra based on the C-band weather radars.

The contribution of radial wind to the measured Doppler velocities was removed to obtain an estimate of the hydrometeor fall velocities. This removal facilitates the investigation of the relationship between polarimetric signatures and fall velocities, enabling a more precise characterization of hydrometeors within the profiler resolution volume. Several methodologies for this removal were investigated. One method assumed the smallest particles could serve as passive tracers to remove the radial wind component from the profiler data (Section 2.4). Using reflectivity to separate terminal fall velocities and radial wind is used in other studies (Orr & Kropfli, 1999; Williams et al., 2000). However, the threshold representing the "smallest" particles significantly impacted our results, as the set threshold introduces variability. Nonetheless, this methodology was applied for the six study cases.

In this study, we also used dual-wavelength spectral reflectivity ratios from the profiler, which, in the case of rainfall, can identify the Mie Notch. Although we did not use the $S_{DWR}$ as the primary separation method, we demonstrated its potential as a performance check for other techniques, such as using the smallest particles as tracers. The discrepancy between theoretical and observed Mie Notch values reflects the influence of wind speed; however, this method is only effective during rainfall. Additionally, differences in attenuation between horizontal and vertical polarizations, or between Ka- and W-band frequencies, can impact the magnitude of the spectra. However, for the applications in our study, the shape of the spectra is more significant than its magnitude. Even though differential attenuation may cause a uniform shift in the spectrum, it does not change the shape. Although differences in spectral broadening in Ka and W bands due to differences in beam widths might influence the shape of the DWR spectra, its effect is expected to be minimal for the purpose of our manuscript as our focus is on the location of the Mie notch rather than its magnitude or width.

We tried using the profiler's default noise threshold (the first non-NaN value), but this threshold was too low as wind interference remained noticeable (Figure B1). Radial wind velocities derived from wind profiles estimated by the Herwijnen radar and the HARMONIE model are used as reference in this study. However, both sources tend to underestimate high wind velocities and variation as a function of height because their lower spatiotemporal resolution cannot capture these dynamics (Figure 3). Accurate removal of the radial wind component is particularly crucial in these cases since the Mie notch cannot be used to identify the radial wind component in case of snow.

We also considered data from the C-band weather radar in Den Helder, yielding simultaneous observations from three radars (the profiler and two C-band radars). However, due to the large distance to Den Helder, the numbers of overlapping observations were very limited and would require interpolation and assumptions to retrieve high-resolution wind fields. Consequently, with the current set-up, our study cannot confirm the best threshold for separating radial wind from terminal fall velocities for (wet) snow. Another potential application of the profiler is emphasized here: by incorporating azimuthal scans into the measurement setup, horizontal wind profiles can be retrieved (Dias Neto et al., 2023). This capability allows for the evaluation of the threshold technique in (wet) snow conditions.

Another complication is that our method does not account for wind variability within a single measurement bin or for vertical wind. Consequences are limited for stratiform events (Atlas et al., 1973; Williams, 2002), such as the first three cases (Figures 4–6). However, when high and variable wind velocities are present, spectral broadening is a serious issue especially for snow (Newman et al., 2009; Testik & Bolek, 2023, and Figures 8 and 9). Methods to address spectral broadening can involve machine learning (Billault-Roux et al., 2023) or a Gaussian convolution kernel can be used to account for spectral broadening (Doviak & Zrnic, 2006; Unal, 2015).

Including wet snow was important as omitting it results in significant overestimation of the mixing ratios of other hydrometeor types in the melting layer. However, we did not simulate spectra for wet snow due to high liquid water content variability within the melting layer and lack of representation in the scattering database. Identifying a representative particle and a method to account for liquid water content could enable this simulation potentially confirming the bimodal shape of the measured spectra in Figure 5e. An in-depth study is required to unravel which precipitation particle in the scattering database best represents the scattering of wet snow.

Lastly, we use relatively "simple" parameterizations to simulate terminal fall velocity of raindrops to be consistent with the HARMONIE weather model. This relationship is less accurate in case of large raindrops as prominent in Figure 7. For large raindrops, Beard's relation is recommended as the fall velocity is known to have an asymptote for large particle sizes (Beard, 1976). More general, we recommend studying the uncertainty related to our parameterizations regarding PSDs, terminal fall velocities, and mass-diameter relations. Sensitivity could be assessed by comparing several empirical relationships and general parameterizations (for instance Böhm, 1989; Garrett et al., 2012; Hoover et al., 2021; Moisseev & Chandrasekar, 2007).

In light rain (Figures 4–6), the spectral differential reflectivity exhibits a relatively uniform signature at low to moderate estimated fall velocities, followed by an increase at higher velocities. In this high fall velocity regime, the calibrated $S_{DR}$ values are influenced by the assumed axis ratio-diameter relationship and the canting angle distribution (Unal & Brule, 2024). Figure 7 presents a case of mixed-phase precipitation, where $S_{DR}$ elevated values at low fall velocities suggest the presence of small oblate ice particles. For the snow case shown in Figure 8, the differential reflectivity spectrogram remains relatively flat with respect to fall velocity in the lowest kilometer consistent with HMC indicating snow aggregates and possibly spherical graupel. Between 3 and 4 km altitude, corresponding to temperatures between −10°C and −15°C an increase in $S_{DR}$ at small fall velocities suggests the presence of small oblate ice particles, likely dendrites.

This study did not examine the effects of parameter variations presented in Table 2. Future research could explore the impact of these variations through a sensitivity analysis. Instead, our study explored the general use of a profiler at a slant angle and its implications, such as removing the radial wind component. Future research could focus on specific identified challenges, such as further examining polarimetric signals of (snow) particles and mixed-phase precipitation.

## 5. Conclusions

This study presents a novel method for quality assessment of an HMC scheme applied to C-band weather radar data, illustrated using six case studies from various seasons and weather conditions in the Netherlands. Utilizing a single Doppler-polarimetric profiler at a slant elevation angle, we retrieved both dual-polarization variables and Doppler spectral characteristics across an entire profile with high temporal and spatial resolution. The most important findings can be summarized as follows:

- The proposed method gives valuable insight into the quality of the HMC scheme for different cases.
- Due to the 45° elevation angle, we are able to retrieve meaningful insights from polarimetric variables.
- The profiler's dual-frequency capability allowed us to detect the Mie notch in case of rain, which is particularly useful for identifying the radial wind component—a challenge posed by the slant angle.
- The vertical cross section retrieved from the profiler reveals many precipitation characteristics. One example is the location of the melting layer, which can easily be identified due to both a large increase in velocity as well as reflectivity.
- For stratiform events, the results are already promising because the limited wind effects allow for clear spectral differences between liquid and frozen particles. The HMC scheme often accurately identifies the melting layer, indicated by reduced probabilities for solid hydrometeor types and increased probabilities for liquid hydrometeors or wet snow.
- Omitting wet snow results in significant overestimation of the mixing ratios of other hydrometeor types especially during stratiform events. Hence, the inclusion of wet snow is essential for accurate mixing ratio retrieval. Future research enabling the inclusion of wet snow scattering properties is highly recommended.

Further research is needed to identify radial wind for snow and to account for turbulence- and shear-induced spectral broadening for all hydrometeor types and to develop a more sophisticated method to automate the process of evaluating an HMC scheme. Lastly, we highly recommend the inclusion of more polarimetric variables from the profiler, such as the spectral correlation coefficient and spectral differential phase.

## Appendix A: Equations for Deriving Mixing Ratios

Given the probabilities ($P_\mathrm{i}$) and measured reflectivity ($Z$), the corresponding mixing ratio ($r_\mathrm{i}$) can be computed. Here, we demonstrate how the mixing ratios for snow ($r_\mathrm{s}$) are derived, the other hydrometeor types following the same logic. First, we use that the total measured reflectivity ($Z$) is defined as Equation 15:

$$Z = Z_\mathrm{r} + Z_\mathrm{ws} + Z_\mathrm{s} + Z_\mathrm{gr}. \tag{A1}$$

Subsequently, we assume that the ratio of the mixing ratios of the hydrometeor types is equal to the ratio of the probabilities, as stated in Equation 14 and repeated over here for convenience:

$$\frac{r_\mathrm{i}}{r_\mathrm{j}} = \frac{P_\mathrm{i}}{P_\mathrm{j}}. \tag{A2}$$

Lastly, we rewrite Equation 11 to express the reflectivity of a certain hydrometeor type ($Z_\mathrm{i}$) as a function of the mixing ratio, which in the case of snow yields:

$$Z_\mathrm{s} = \left(\frac{r_\mathrm{s}}{A_\mathrm{s}}\right)^{\frac{1}{B_\mathrm{s}}}. \tag{A3}$$

Combining the previous equations and assumptions, we can rewrite Equation A1 as

$$Z = Z_\mathrm{s} + c_1 Z_\mathrm{s}^{c_2} + c_3 Z_\mathrm{s}^{c_4} + c_5 Z_\mathrm{s}^{c_6}, \tag{A4}$$

with $0 \le Z_\mathrm{s} \le Z$ and exponents $\mathrm{C}_1$ to $\mathrm{C}_6$ defined as

$$C_1 = \left(\frac{P_\mathrm{r} A_\mathrm{s}}{P_\mathrm{s} A_r}\right)^{\frac{1}{B_r}}, C_2 = \frac{B_s}{B_r}, C_3 = \left(\frac{P_g A_\mathrm{s}}{P_\mathrm{s} A_\mathrm{g}}\right)^{\frac{1}{B_\mathrm{g}}}, C_4 = \frac{B_\mathrm{s}}{B_\mathrm{g}}, C_5 = \left(\frac{P_\mathrm{ws} A_\mathrm{s}}{P_\mathrm{s} A_\mathrm{ws}}\right)^{\frac{1}{B_\mathrm{ws}}}, C_6 = \frac{B_\mathrm{s}}{B_\mathrm{ws}} \tag{A5}$$

Equation A4 has to be solved numerically. Once $Z_s$ is calculated, we can compute $r_s$ using Equation 11. Similarly, $Z_{ws}$ and $Z_{gr}$ are obtained. Finally, $Z_r$ is computed from Equation A1.

## Appendix B: Predefined Noise Threshold Profiler

Instead of defining a threshold to identify the smallest particles, we tried implementing the predefined threshold provided in the profiler observations (Figure B1). Compared to Figure 4c, the highest reflectivity values (above 20 dB*S*) are shifted from around $-4$ m s$^{-1}$ to $-7.5$ m s$^{-1}$ (Figure B1a). Compared to Figure 9b, the highest reflectivity values (above 18 dB*S*) are shifted from a maximum adjusted velocity of $-6$ m s$^{-1}$ in the lowest 750 to $-17$ m s$^{-1}$ (Figure B1b). These velocities are too high for the precipitation types of that day (light rain on 3 February and snow on 31 March), indicating this predefined threshold is not suitable to remove the radial wind component.

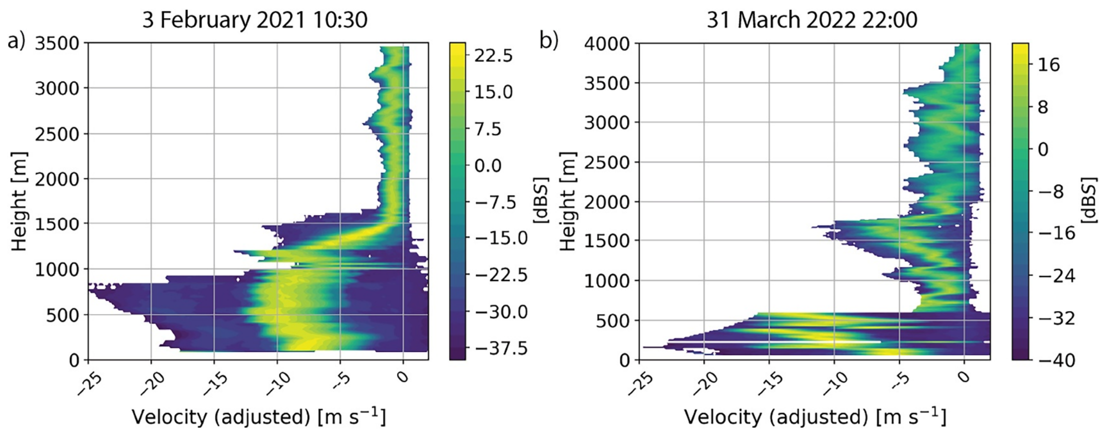


**Figure B1.** (a) Spectrogram from profiler observations at one time step (10:30). Radial velocity (*x*-axis) adjusted for the wind component using the predefined noise threshold from the profiler. (b) Same as panel (a) but for 31 March 2021.

## Data Availability Statement

The volumetric radar data are publicly available on the KNMI Data Platform (2025). Please note this data set is in KNMI-HDF5 format. Conversions are needed to obtain the data in hybrid KNMI-ODIM HDF5 format, which is required as input for the HMC scheme.

**Acknowledgments**

We acknowledge financial support from the Dutch Research Council (NWO) through project ALWGO.2018.048 and the KNMI's multiannual strategic research program (project name: "A Seamless Connection of Nowcasting with Probabilistic Forecasting of Clouds and Precipitation"). Furthermore, this manuscript has been accomplished using data from the Ruisdael Observatory, a scientific research infrastructure which is (partly) financed by the NWO (Grant 184.034.015). We thank the two anonymous reviewers for their constructive comments and suggestions.

## References

Al-Sakka, H., Boumahmoud, A.-A., Fradon, B., Frasier, S. J., & Tabary, P. (2013). A new fuzzy logic hydrometeor classification scheme applied to the French X-C-and S-band polarimetric radars. *Journal of Applied Meteorology and Climatology*, *52*(10), 2328–2344. https://doi.org/10.1175/JAMC-D-12-0236.1

Andsager, K., Beard, K. V., & Laird, N. F. (1999). Laboratory measurements of axis ratios for large raindrops. *Journal of the Atmospheric Sciences*, *56*(15), 2673–2683. https://doi.org/10.1175/1520-0469(1999)056⟨2673:LMOARF⟩2.0.CO;2

Argence, S., Lambert, D., Richard, E., Chaboureau, J.-P., & Söhne, N. (2008). Impact of initial condition uncertainties on the predictability of heavy rainfall in the mediterranean: A case study [_eprint: ]. *Quarterly Journal of the Royal Meteorological Society*, *134*(636), 1775–1788. https://onlinelibrary.wiley.com/doi/pdf/10.1002/qj.314

Atlas, D., Srivastava, R. C., & Sekhon, R. S. (1973). Doppler radar characteristics of precipitation at vertical incidence. *Reviews of Geophysics*, *11*(1), 1–35. https://doi.org/10.1029/RG011i001p00001

Baldini, L., & Gorgucci, E. (2006). Identification of the melting layer through dual-polarization radar measurements at vertical Incidence. *Journal of Atmospheric and Oceanic Technology*, *23*(6), 829–839. https://doi.org/10.1175/JTECH1884.1

Battan, L. J. (1973). *Radar observation of the atmosphere*. University of Chicago Press.

Beard, K. V. (1976). Terminal velocity and shape of cloud and precipitation drops aloft [Publisher: American meteorological society section: Journal of the atmospheric sciences]. *Journal of the Atmospheric Sciences*, *33*(5), 851–864. https://doi.org/10.1175/1520-0469(1976)033⟨0851:TVASOC⟩2.0.CO;2

Beekhuis, H., & Mathijssen. (2018). From pulse to product, highlights of the upgrade project of the Dutch national weather radar network. *ERAD2018*, 960–965. https://doi.org/10.18174/454537

Bengtsson, L., Andrae, U., Aspelien, T., Batrak, Y., Calvo, J., Rooy, W. d., et al. (2017). The HARMONIE–AROME model configuration in the ALADIN–HIRLAM NWP system [Publisher: American meteorological society section: Monthly weather review]. *Monthly Weather Review*, *145*(5), 1919–1935. https://doi.org/10.1175/MWR-D-16-0417.1

Berne, A., Delrieu, G., Creutin, J.-D., & Obled, C. (2004). Temporal and spatial resolution of rainfall measurements required for urban hydrology. *Journal of Hydrology*, *299*(3), 166–179. https://doi.org/10.1016/j.jhydrol.2004.08.002

Besic, N., Figueras I Ventura, J., Grazioli, J., Gabella, M., Germann, U., & Berne, A. (2016). Hydrometeor classification through statistical clustering of polarimetric radar measurements: A semi-supervised approach. *Atmospheric Measurement Techniques*, *9*(9), 4425–4445. https://doi.org/10.5194/amt-9-4425-2016

Billault-Roux, A.-C., Ghiggi, G., Jaffeux, L., Martini, A., Viltard, N., & Berne, A. (2023). Dual-frequency spectral radar retrieval of snowfall microphysics: A physics-driven deep-learning approach [Publisher: Copernicus GmbH]. *Atmospheric Measurement Techniques*, *16*(4), 911–940. https://doi.org/10.5194/amt-16-911-2023

Bogerd, L., Leijnse, H., Overeem, A., & Uijlenhoet, R. (2024). Assessing sampling and retrieval errors of GPROF precipitation estimates over The Netherlands. *Atmospheric Measurement Techniques*, *17*(1), 247–259. https://doi.org/10.5194/amt-17-247-2024

Bogerd, L., Overeem, A., Leijnse, H., & Uijlenhoet, R. (2021). A comprehensive five-year evaluation of IMERG late run precipitation estimates over The Netherlands. *Journal of Hydrometeorology*, *22*(7), 1855–1868. https://doi.org/10.1175/JHM-D-21-0002.1

Böhm, H. P. (1989). A general equation for the terminal fall speed of solid hydrometeors [Publisher: American meteorological Society section: Journal of the atmospheric sciences]. *Journal of the Atmospheric Sciences*, *46*(15), 2419–2427. https://doi.org/10.1175/1520-0469(1989)046⟨2419:AGEFTT⟩2.0.CO;2

Bringi, V. N., & Chandrasekar, V. (2001). *Polarimetric Doppler weather radar: Principles and applications*. Cambridge University Press.

Caniaux, G. (1993). Parame´trisation de la phase glace dans un mode`le non hydrostatique de nuage: Application a` une ligne de grains tropicale: [the`se en partie soutenue sur un ensemble de travaux] [These de doctorat]. Toulouse 3. Retrieved August 2, 2024, from https://theses.fr/1993TOU30071

Caniaux, G., Redelsperger, J.-L., & Lafore, J.-P. (1994). A a numerical study of the stratiform region of a fast-moving squall line. Part I: General description and water and heat budgets [Publisher: American meteorological society section: Journal of the atmospheric sciences]. *Journal of the Atmospheric Sciences*, *51*(14), 2046–2074. https://doi.org/10.1175/1520-0469(1994)051⟨2046:ANSOTS⟩2.0.CO;2

Chaubey, I., Haan, C. T., Grunwald, S., & Salisbury, J. M. (1999). Uncertainty in the model parameters due to spatial variability of rainfall. *Journal of Hydrology*, *220*(1), 48–61. https://doi.org/10.1016/S0022-1694(99)00063-3

Chen, C., Unal, C. M. H., & Nijhuis, A. C. P. O. (2022). Jensen–Shannon distance-based filter and unsupervised evaluation metrics for polarimetric weather radar processing. *IEEE Transactions on Geoscience and Remote Sensing*, *60*, 1–18. https://doi.org/10.1109/TGRS.2022.3200731

Cifelli, R., & Chandrasekar, V. (2010). Dual-polarization radar rainfall estimation. In *Rainfall: State of the Science* (pp. 105–125). American Geophysical Union (AGU). https://doi.org/10.1029/2010GM000930

Dias Neto, J., Nuijens, L., Unal, C., & Knoop, S. (2023). Combined wind lidar and cloud radar for high-resolution wind profiling. *Earth System Science Data*, *15*(2), 769–789. https://doi.org/10.5194/essd-15-769-2023

Doviak, R. J., & Zrnic, D. S. (2006). *Doppler radar and weather observations* (Second). Dover publications.

Ekelund, R., Brath, M., Mendrok, J., & Eriksson, P. (2020). ARTS microwave single scattering properties database. https://doi.org/10.5281/zenodo.4646605

Engdahl, B. J. K., Thompson, G., & Bengtsson, L. (2020). Improving the representation of supercooled liquid water in the HARMONIE-AROME weather forecast model. *Tellus A: Dynamic Meteorology and Oceanography*, *72*(1), 1–18. https://doi.org/10.1080/16000870.2019.1697603

Eriksson, P., Ekelund, R., Mendrok, J., Brath, M., Lemke, O., & Buehler, S. A. (2018). A general database of hydrometeor single scattering properties at microwave and sub-millimetre wavelengths. *Earth System Science Data*, *10*(3), 1301–1326. https://doi.org/10.5194/essd-10-1301-2018

Fabry, F. (2015). *Radar meteorology: Principles and practice*. Cambridge University Press. https://doi.org/10.1017/CBO9781107707405

Fabry, F., & Zawadzki, I. (1995). Long-term radar observations of the melting layer of precipitation and their interpretation [Publisher: American meteorological society section: Journal of the atmospheric sciences]. *Journal of the Atmospheric Sciences*, *52*(7), 838–851. https://doi.org/10.1175/1520-0469(1995)052⟨0838:LTROOT⟩2.0.CO;2

Falconi, M. T., Vulpiani, G., Montopoli, M., & Marzano, F. S. (2015). C-band polarimetric weather radar calibration using a fuzzy logic fusion of three techniques. In *2015 IEEE International Geoscience and Remote Sensing Symposium (IGARSS)* (pp. 5363–5366). https://doi.org/10.1109/IGARSS.2015.7327047

Foote, G. B., & du Toit, P. S. (1969). Terminal velocity of raindrops aloft. *Journal of Applied Meteorology and Climatology*, *8*(2), 249–253. https://doi.org/10.1175/1520-0450(1969)008⟨0249:TVORA⟩2.0.CO;2

Fukao, S., Hamazu, K., & Doviak, R. J. (2014). *Radar for meteorological and atmospheric observations*. Springer.

Gao, S., & Li, X. (2008). Impacts of initial conditions on cloud-resolving model simulations. *Advances in Atmospheric Sciences*, *25*(5), 737–747. https://doi.org/10.1007/s00376-008-0737-6

Garrett, T. J., Fallgatter, C., Shkurko, K., & Howlett, D. (2012). Fall speed measurement and high-resolution multi-angle photography of hydrometeors in free fall. *Atmospheric Measurement Techniques*, *5*(11), 2625–2633. https://doi.org/10.5194/amt-5-2625-2012

Grazioli, J., Tuia, D., & Berne, A. (2015). Hydrometeor classification from polarimetric radar measurements: A clustering approach. *Atmospheric Measurement Techniques*, *8*(1), 149–170. https://doi.org/10.5194/amt-8-149-2015

Hall, W., Rico-Ramirez, M. A., & Krämer, S. (2015). Classification and correction of the bright band using an operational C-band polarimetric radar. *Journal of Hydrology*, *531*, 248–258. https://doi.org/10.1016/j.jhydrol.2015.06.011

Harrison, D. L., Driscoll, S. J., & Kitchen, M. (2000). Improving precipitation estimates from weather radar using quality control and correction techniques. *Meteorological Applications*, *7*(2), 135–144. https://doi.org/10.1017/S1350482700001468

Heistermann, M., Jacobi, S., & Pfaff, T. (2013). Technical Note: An open source library for processing weather radar data wradlib. *Hydrology and Earth System Sciences*, *17*(2), 863–871. https://doi.org/10.5194/hess-17-863-2013

Holleman, I. (2005). Quality control and verification of weather radar wind profiles [publisher: American meteorological society section: Journal of atmospheric and oceanic technology]. *Journal of Atmospheric and Oceanic Technology*, *22*(10), 1541–1550. https://doi.org/10.1175/JTECH1781.1

Hong, S.-Y., Dudhia, J., & Chen, S.-H. (2004). A revised approach to ice microphysical processes for the bulk parameterization of clouds and precipitation. *Monthly Weather Review*, *132*(1), 103–120. https://doi.org/10.1175/1520-0493(2004)132⟨0103:ARATIM⟩2.0.CO;2

Hoover, J., Earle, M. E., Joe, P. I., & Sullivan, P. E. (2021). Unshielded precipitation gauge collection efficiency with wind speed and hydrometeor fall velocity. *Hydrology and Earth System Sciences*, *25*(10), 5473–5491. https://doi.org/10.5194/hess-25-5473-2021

Karrer, M., Dias Neto, J., von Terzi, L., & Kneifel, S. (2022). Melting behavior of rimed and unrimed snowflakes investigated with statistics of triple-frequency Doppler radar observations. *Journal of Geophysical Research: Atmospheres*, *127*(9), e2021JD035907. https://doi.org/10.1029/2021JD035907

KNMI Data Platform. (2025). Precipitation - Radar 5 minute full volume data Herwijnen - Archive [Dataset]. *KNMI Data Platform*. Retrieved from https://dataplatform.knmi.nl/dataset/radar-tar-vol-full-herwijnen-1-0

Kollias, P., Albrecht, B. A., & Marks, F. (2002). Why Mie? Accurate observations of vertical air velocities and raindrops using a cloud radar [publisher: American meteorological Society section: Bulletin of the American meteorological society]. *Bulletin of the American Meteorological Society*, *83*(10), 1471–1484. https://doi.org/10.1175/BAMS-83-10-1471

Kollias, P., Rémillard, J., Luke, E., & Szyrmer, W. (2011). Cloud radar Doppler spectra in drizzling stratiform clouds: 1. Forward modeling and remote sensing applications. *Journal of Geophysical Research*, *116*(D13), D13201. https://doi.org/10.1029/2010JD015237

Kumjian, M. R. (2018). Weather radars. In C. Andronache (Ed.), *Remote Sensing of Clouds and Precipitation* (pp. 15–63). Springer International Publishing. Retrieved May 20, 2024, from. https://doi.org/10.1007/978-3-319-72583-3

Liebe, H. J., Hufford, G. A., & Manabe, T. (1991). A model for the complex permittivity of water at frequencies below 1 THz. *International Journal of Infrared and Millimeter Waves*, *12*(7), 659–675. https://doi.org/10.1007/BF01008897

Lim, S., Chandrasekar, V., & Bringi, V. (2005). Hydrometeor classification system using dual-polarization radar measurements: Model improvements and in situ verification. *IEEE Transactions on Geoscience and Remote Sensing*, *43*(4), 792–801. https://doi.org/10.1109/TGRS.2004.843077

Liu, H., & Chandrasekar, V. (2000). Classification of hydrometeors based on polarimetric radar measurements: Development of fuzzy logic and neuro-fuzzy systems, and in situ verification. *Journal of Atmospheric and Oceanic Technology*, *17*(2), 140–164. https://doi.org/10.1175/1520-0426(2000)017⟨0140:COHBOP⟩2.0.CO;2

Liu, J. Y., & Orville, H. D. (1969). Numerical modeling of precipitation and cloud shadow effects on mountain-induced cumuli. *Journal of the Atmospheric Sciences*, *26*(6), 1283–1298. https://doi.org/10.1175/1520-0469(1969)026⟨1283:NMOPAC⟩2.0.CO;2

Locatelli, J. D., & Hobbs, P. V. (1974). Fall speeds and masses of solid precipitation particles. *Journal of Geophysical Research*, *79*(15), 2185–2197. https://doi.org/10.1029/JC079i015p02185

Mak, H. Y. L., & Unal, C. (2025). Peering into the heart of thunderstorm clouds: Insights from cloud radar and spectral polarimetry. *Atmospheric Measurement Techniques*, *18*(5), 1209–1242. https://doi.org/10.5194/amt-18-1209-2025

Mätzler, C. (2006). *Thermal microwave radiation: Applications for remote sensing* (Vol. 52). IET. https://doi.org/10.1049/PBEW052E

Mishchenko, M. I. (2000). Calculation of the amplitude matrix for a nonspherical particle in a fixed orientation. *Applied Optics*, *39*(6), 1026–1031. https://doi.org/10.1364/AO.39.001026

Moisseev, D. N., & Chandrasekar, V. (2007). Nonparametric estimation of raindrop size distributions from dual-polarization radar spectral observations. *Journal of Atmospheric and Oceanic Technology*, *24*(6), 1008–1018. https://doi.org/10.1175/JTECH2024.1

Mühlbauer, K., Heistermann, M., & Goudenhoofdt, E. (2020). Wradlib v1.9.0. https://doi.org/10.5281/zenodo.4290240.Accessedon10June2024

Newman, A. J., Kucera, P. A., Williams, C. R., & Bliven, L. F. (2009). Snowflake size spectra retrieved from a UHF vertical profiler. *Journal of Atmospheric and Oceanic Technology*, *26*(2), 180–199. https://doi.org/10.1175/2008JTECHA1105.1

Orr, B. W., & Kropfli, R. A. (1999). A method for estimating particle fall velocities from vertically pointing Doppler radar. *Journal of Atmospheric and Oceanic Technology*, *16*(1), 29–37. https://doi.org/10.1175/1520-0426(1999)016⟨0029:AMFEPF⟩2.0.CO;2

Overeem, A., de Vries, H., Al Sakka, H., Uijlenhoet, R., & Leijnse, H. (2021). Rainfall-induced attenuation correction for two operational dual-polarization C-band radars in the Netherlands [Publisher: American meteorological society section: Journal of atmospheric and oceanic technology]. *Journal of Atmospheric and Oceanic Technology*, *38*(6), 1125–1142. https://doi.org/10.1175/JTECH-D-20-0113.1

Overeem, A., Holleman, I., & Buishand, A. (2009). Derivation of a 10-year radar-based climatology of rainfall. *Journal of Applied Meteorology and Climatology*, *48*(7), 1448–1463. https://doi.org/10.1175/2009JAMC1954.1

Overeem, A., Uijlenhoet, R., & Leijnse, H. (2020). Full-year evaluation of nonmeteorological echo removal with dual-polarization fuzzy logic for two C-band radars in a temperate climate. *Journal of Atmospheric and Oceanic Technology*, *37*(9), 1643–1660. https://doi.org/10.1175/JTECH-D-19-0149.1

Pruppacher, H. R., & Klett, J. D. (2010). *Microphysics of clouds and precipitation* (2nd ed.). Springer.

Rauber, R. M., & Nesbitt, S. W. (2018). *Radar meteorology: A first course* (1st ed.). John Wiley and Sons. https://doi.org/10.1002/9781118432662

Ryzhkov, A. V., Diederich, M., Zhang, P., & Simmer, C. (2014). Potential utilization of specific attenuation for rainfall estimation, mitigation of partial beam blockage, and radar networking. *Journal of Atmospheric and Oceanic Technology*, *31*(3), 599–619. https://doi.org/10.1175/JTECH-D-13-00038.1

Ryzhkov, A. V., & Zrnic, D. S. (2019). *Radar polarimetry for weather observations*. Springer International Publishing. https://doi.org/10.1007/978-3-030-05093-1

Schmidt, M., Trömel, S., Ryzhkov, A. V., & Simmer, C. (2018). Severe hail detection: Hydrometeor classification for polarimetric c-band radars using fuzzy-logic and t-matrix scattering simulations [ISSN: 2155-5753]. *2018 19th International Radar Symposium (IRS)*, 1–7. https://doi.org/10.23919/IRS.2018.8448037

Schuur, T., Heinselman, P., & Scharfenberg, K. (2003). Overview of the Joint Polarization Experiment (JPOLE) *(NOAA/NSSL Report)*. NOAA and University of Oklahoma. Oklahoma.

Seliga, T. A., & Bringi, V. N. (1976). Potential use of radar differential reflectivity measurements at orthogonal polarizations for measuring precipitation. *Journal of Applied Meteorology and Climatology*, *15*(1), 69–76. https://doi.org/10.1175/1520-0450(1976)015⟨0069:PUORDR⟩2.0.CO;2

Straka, J. M., Zrnić, D. S., & Ryzhkov, A. V. (2000). Bulk hydrometeor classification and quantification using polarimetric radar data: Synthesis of relations. *Journal of Applied Meteorology and Climatology*, *39*(8), 1341–1372. https://doi.org/10.1175/1520-0450(2000)039⟨1341:BHCAQU⟩2.0.CO;2

Testik, F. Y., & Bolek, A. (2023). Wind and turbulence effects on raindrop fall speed. *Journal of the Atmospheric Sciences*, *80*(4), 1065–1086. https://doi.org/10.1175/JAS-D-22-0137.1

Tridon, F., & Battaglia, A. (2015). Dual-frequency radar Doppler spectral retrieval of rain drop size distributions and entangled dynamics variables. *Journal of Geophysical Research: Atmospheres*, *120*(11), 5585–5601. https://doi.org/10.1002/2014JD023023

Unal, C. (2015). High-resolution raindrop size distribution retrieval based on the Doppler spectrum in the case of slant profiling radar. *Journal of Atmospheric and Oceanic Technology*, *32*(6), 1191–1208. https://doi.org/10.1175/JTECH-D-13-00225.1

Unal, C., & Brule, Y. v. d. (2024). Exploring millimeter-wavelength radar capabilities for raindrop size distribution retrieval: Estimating mass-weighted mean diameter from the differential backscatter phase. *Journal of Atmospheric and Oceanic Technology*, *41*(6), 583–603. https://doi.org/10.1175/JTECH-D-23-0094.1

Williams, C. R. (2002). Simultaneous ambient air motion and raindrop size distributions retrieved from UHF vertical incident profiler observations [Conference Name: Radio Science]. *Radio Science*, *37*(2), 1–22. https://doi.org/10.1029/2000RS002603

Williams, C. R., Ecklund, W. L., Johnston, P. E., & Gage, K. S. (2000). Cluster analysis techniques to separate air motion and hydrometeors in vertical incident profiler observations. *Journal of Atmospheric and Oceanic Technology*, *17*(7), 949–962. https://doi.org/10.1175/1520-0426(2000)017⟨0949:CATTSA⟩2.0.CO;2

Yanovsky, F. J., Pitertsev, A. A., Unal, C. M. H., & Russchenberg, H. W. J. (2023). Peculiarities and experience of W-band cloud radar calibration. *2023 Signal Processing Symposium (SPSympo)*, 208–213. https://doi.org/10.23919/SPSympo57300.2023.10302660

Yuter, S. E., Kingsmill, D. E., Nance, L. B., & Löffler-Mang, M. (2006). Observations of precipitation size and fall speed characteristics within coexisting rain and wet snow. *Journal of Applied Meteorology and Climatology*, *45*(10), 1450–1464. https://doi.org/10.1175/JAM2406.1

Zawadzki, I., Jung, E., & Lee, G. (2010). Snow studies. Part I: A study of natural variability of snow terminal velocity. *Journal of the Atmospheric Sciences*, *67*(5), 1591–1604. https://doi.org/10.1175/2010JAS3342.1

Zheng, H., Zhang, Y., Li, H., Wu, Z., & Zhou, Z. (2023). Revisiting raindrop axis ratios based on 3D oblate spheroidal reconstruction: 2D video disdrometer observations during tropical cyclone passages. *Geophysical Research Letters*, *50*(9), e2023GL103281. https://doi.org/10.1029/2023GL103281

Zrnić, D. S., Ryzhkov, A., Straka, J., Liu, Y., & Vivekanandan, J. (2001). Testing a procedure for automatic classification of hydrometeor types. *Journal of Atmospheric and Oceanic Technology*, *18*(6), 892–913. https://doi.org/10.1175/1520-0426(2001)018⟨0892:TAPFAC⟩2.0.CO;2